



# Dynamic plastic response of sandwich structures with graded polyurethane foam cores and metallic face sheets exposed to uniform blast loading: experimental study and numerical simulation

R. Khondabi<sup>1</sup> · H. Khodarahmi<sup>1</sup> · R. Hosseini<sup>1</sup> · M. Ziya-Shamami<sup>1</sup>

Received: 8 November 2022 / Accepted: 28 July 2023 / Published online: 17 September 2023  
© The Author(s), under exclusive licence to The Brazilian Society of Mechanical Sciences and Engineering 2023

## Abstract

In the current research study, the blast performance of sandwich panels with graded polyurethane foam core and aluminum face sheets with the same mass and different layering arrangements was studied experimentally and numerically. An explosive shock tube apparatus was employed to conduct the blast tests. The metallic sandwich panels with single-layer, double- and triple-layered cores were designed and fabricated at ambient pressure. The maximum displacements of face sheets at the center were measured in the experiments. All the sandwich panels exhibited a similar plastic deformation mode, which was characterized by a uniform global dome with the maximum transverse deflection taking place at the center of the panel. The ANSYS/Autodyn finite element code was also employed for further discussion on the structural response, fluid–structure interaction effect, deformation pattern, velocity response, and energy absorption capacity of the sandwich panels. For the validation of the numerical model, the simulation results in terms of the displacement of back and front face sheets at the center were compared with the corresponding experimental data. The results indicated that the graded foam core strategy would greatly affect the level of plastic deformation of the back face sheets. It was also concluded that in comparison with the back face sheet deflection of the P1MT30 (single-layer core) configuration, P3HMLT30 (triple-layered core with relative densities in descending order) and P2HLT30 (double-layered core) configurations gave a decrease by 16.8% and 8.3%, respectively, while P2LHT30 (double-layered core with relative densities in ascending order) and P3LMHT30 configurations gave an increase by 15.4% and 25%, respectively. Also, by consideration of total energy dissipation as a criterion of blast performance, the results showed that the energy absorption of P3HMLT30 and P2HLT30 configurations were reduced by 30.2% and 13.8%, respectively, compared to the P1MT30 panel.

**Keywords** ANSYS/Autodyn software · Aluminum plate · Energy absorption · Uniform blast loading · Polyurethane · Shock tube

## 1 Introduction

Over the past decade, sandwich panels made from fiber-reinforced polymer (FRP) or metallic face sheets separated by a core have had wide and extensive considerable applications in various industries, such as naval, sporting goods, building, aerospace, and automobile [1–3]. This issue can be owing to their noteworthy characteristics in terms of low thermal conductivity, aerodynamic

smoothness, stiffness-to-weight and high strength ratios, ease of manufacture, impressive acoustic insulation, and design ability compared to other structures like monolithic and multi-layered plates [4–9]. The mentioned unique properties have proposed sandwich panels as an ideal structure component to construct modern light-weight composite tubes and shells, roof panels, and cladding walls with high structural efficiency, particularly while they are subjected to extreme dynamic loads such as air blasts. For the case of uniform blast loading tests, the features result in the dispersion of the shock transmitted to the panel and thus protect anything placed behind it. It is noteworthy to mention that the amount of explosive energy transmitted to the sandwich panel exposed to compression loading is controlled by the stress–strain curve of the low-density foam core [10–12]. As a result, changing the mass and equivalent stiffness of the sandwich panel

---

Technical Editor: Aurelio Araujo.

---

✉ R. Hosseini  
r.hosseini.mech@gmail.com

<sup>1</sup> Department of Mechanical Engineering, Faculty of Engineering, Imam Hossein Comprehensive University, Tehran, Iran

plays a vital role in the plastic deformation and failure pattern of the structure while changing the core properties. Therefore, engineers need to figure out what is the most appropriate core configuration.

During the past 10 years, stepwise graded materials were widely employed as a core in sandwich panels. In these materials, the mechanical properties of the material can vary gradually or layer-by-layer within the material itself [13–15]. Note that due to the design and control of the characteristics and properties of the layered/graded core structure, these materials show great potential to be selected as an effective core material in energy absorption systems. Under such a circumstance, the blast energy is greatly absorbed and the blast resistance of sandwich structures is improved since the face sheets and the core are designed in such a way that the core carries the shear load and the skins carry the bending load. According to the description provided, a great deal of investigation into the dynamic response of sandwich construction has been performed over the past decade [16–22]. A brief review of the related important investigations is given next.

Mostafa et al. [23] conducted a series of experiments on rigid polyurethane foam (RPF) intending to develop a cost-effective lightweight protection method for explosive transporting storage and container facilities. Different densities of RFP were reinforced by 10%, 20%, and 30% of sand particles. To relate the results of indoor blast tests to real-life scenarios, explosive scaling laws were used. Langdon et al. [24, 25] reported an experimental and numerical study on the air blast behavior of sandwich structures with E-glass fiber-reinforced vinyl ester face sheets and PVC foam cores and compared it with the response of equivalent mass composite-only structures made of glass fiber-reinforced vinyl ester. The localized load was generated by the detonation of a plastic explosive (PE4) close to the structure at a standoff distance of 50 mm. The panels exhibited different failure modes by the increase of impulse value such as delamination of the front face sheet, core compression, delamination of the back face sheet, fiber fracture, fragmentation of the core, and debonding between the core and face sheet. Complete core penetration was observed in the sandwich panels, while no penetration happened in the equivalent mass (EM) composite-only panels. EM panels were manufactured using the same composite material as the sandwich panel face sheet. The structures with denser cores represented lower damage levels. It was also reported that EM panels had better performance than the panels with PVC foam core. The performance of PVC foam and aluminum alloy foam (ALPORAS) cored sandwich panels exposed to low-velocity impact loading was investigated both experimentally and numerically by Rajaneesh and his colleagues [26]. Experiments were carried out at an impact velocity of 5.8 m/s by a hemispherical punch of mass 8.7 kg. It was found that the energy absorption and penetration force are increased by

selecting the PVC foam core (H250) instead of the ALPORAS foam core at the same density. Moreover, the mass of the sandwich structure could be decreased using the PVC foam core (H80) instead of the ALPORAS foam core at the same compressive strength.

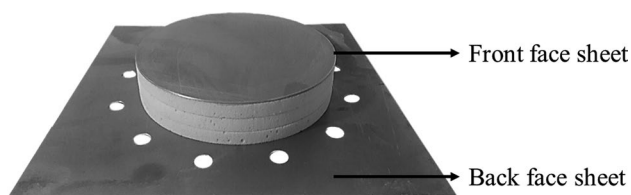
Zhou et al. [27] described the outcomes of a combined numerical study and experimental investigation to assess the perforation performance and resistance of sandwich panels with PVC foam cores. It was found that the characteristics of the foam core strongly affect the perforation performance of plain foams and their sandwich structures. Eventually, it was concluded that compared to sandwich structures tested in the air, panels impacted in a watery environment suggest a lower perforation resistance. Furthermore, in another study presented by Zhou et al. [28], several experiments were conducted on sandwich panels with carbon fiber face sheets and the triple-layered core that was produced by bonding foams of various densities together. It was obtained that most of the structures experienced failure in a through-thickness shearing mode and left an obvious cylindrical hole in the multi-layered core. In 2017, Ye and his colleagues [29] conducted a laboratory-scale experimental investigation on the resistance of clamped sandwich structures with PVC foam cores impacted by metallic foam projectiles. It was figured out that compared to the ascending order of core densities, the descending order has many advantages in the mechanical resistance of the sandwich panel. Dođru and Güzelbey [30] focused on reducing the damage of soldier boots under blast loads by using thermoplastic polyurethane (TPU), Carbon-Kevlar fiber composite (CKF), and multi-walled carbon nanotube (MWCNT) materials to reinforce the boot sole. Polyurethane MWCNT with a weight fraction from 1 to 5% was prepared, and the tensile tests showed that 1% MWCNT had the best mechanical properties. Hence, TPU reinforced with 1% MWCNT along with 10 layers of Carbon-Kevlar fiber composite was selected as the base material for three boot types. The results exhibited that the best reduction in landmine explosion was achieved by approximately 12% with the fully damped soldier boot. Later on, the free air-blast response of steel sandwich structures with three different core materials was investigated to design an armored door with high blast resistance as well as minimum structural weight [31]. The blast response of sandwich panels with vulcanized rubber (VR) and RFP cores was numerically compared with hollow sandwich structures. Different mass ranges of TNT charge from 1 to 10 kg at 1-m standoff distance were tested. The results proved that using the RFP core in the sandwich panel was more efficient than the others where the average permanent transverse deflection of the RFP sandwich panel was, respectively, 49% and 53% less than the VR and hollow sandwich structures. Empirical design formulae were presented based on the parametric numerical study for prediction of the maximum transverse

deflection of the sandwich panels with steel face sheets and different core materials subjected to free air blast loading.

In 2018, Mishra and his colleagues [32] investigated the tensile properties of layered FG polymer nanocomposites based on the ASTM standard D 638–03 for different weight fractions of 0.25 wt.%, 0.5 wt.%, 0.75 wt.% and 1 wt.%. To synthesize the 5-mm-thick FGPNC sheet, the epoxy-alumina nanocomposites were cast in a vertical acrylic mold. For the case of FGPNC, flexural modulus and flexural strength were improved by 23% and 10%, respectively, compared to the layered sample of neat epoxy loading from the neat epoxy side. Besides, these amounts were 17% and 6% when the sample was loaded from the 1 wt.% side. Aydin et al. [33] compared the failure mechanism and deformation mode of FG sandwich panels and aluminum plates under impact loading by a 9-mm Parabellum projectile. It was found that the FG sandwich panel has a better ballistics performance. For multifunctional applications, Hohe et al. [34] worked on the design of FG cellular sandwich cores by performing several experiments and numerical simulations. Two types of particle-based cellular base materials were tested by hollow spheres and particulate advanced pore morphology foams. Lin et al. [35] fabricated an FGM panel using high-density polyethylene and aluminum alloy materials. Axisymmetric bending of the fabricated panels was investigated under different loading conditions using the universal testing machine. Besides, an explicit refined plate theory was extended to accurately predict the thermo-mechanical behavior of the panels. By using a direct method, several formulas were derived to predict the effective stiffness coefficients of composite elastic beams made of FGMs and foams [36]. Garg et al. [37] found that among several material variation laws such as sigmoidal, exponential, and power, sandwich FGM beam having exponentially varying FGM core (C-Type-E1) and ceramic face sheets has the best performance. Jing et al. [38] studied the dynamic response of sandwich beams with metallic skins and three different core configurations under low-velocity impact loading using a drop-weight testing device. Negative and positive layered-gradient cores along with the non-gradient monolithic core were considered in the study. More investigation in this field can be found in Refs. [39–42]. Li et al. [43] investigated

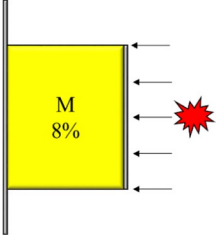
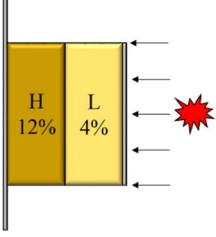
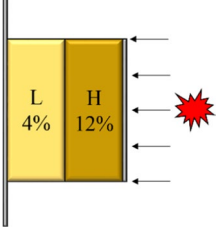
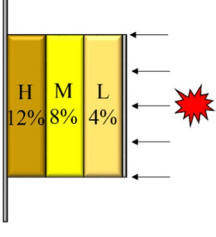
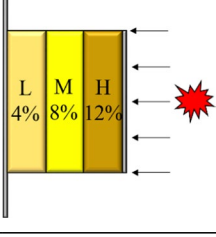
the thermal post-buckling behavior of sandwich structures with functionally graded honeycomb cores. Xiao et al. [44] studied the compression behavior of graded auxetic reentrant honeycomb and presented the deformation mode, crushing stress, and Poisson's ratio distribution. Jin et al. [45] numerically investigated the blast behavior of functionally graded reentrant honeycomb sandwich panels. Numerical results reveal that the specific energy absorption and panel permanent deflections were promoted considerably. Chen et al. [46] investigated the dynamic response and design optimization of clamped sandwich panels with aluminum alloy face sheets and a layered-gradient closed-cell aluminum foam core subjected to air-blast loading. Two surrogate model methods, namely response surface method (RSM) and radial basis function (RBF), were employed to construct objective response functions. The single-objective adaptive response surface method (ARSM) and multi-objective genetic algorithm (MOGA) were also used for the defined optimization problem. The optimization results indicated the trade-off relationships among the minimum deflection, minimum structural mass, and maximum energy absorption. Furthermore, Zhou and Jing [47] studied the dynamic response of clamped square sandwich panel with layered-gradient metal foam core subjected to blast loading. A new yield criterion along with analytical solutions to predict the maximum permanent deflection of the panels was proposed. It was found that the uniform core sandwich panel is better than that of the gradient core one and the negative gradient sandwich panel is superior to that with a positive gradient core in blast resistance for the same equivalent mass. In another related study by this research group, Jing et al. [48] found that all the layered-gradient core sandwich panels have a weaker blast resistance capability than the ungraded sandwich panels because of the reduction in the structural integrity of the specimens. For a given effective impulse, the specific energy absorption value of the positive gradient sandwich panels is the largest, followed by that of the ungraded sandwich panels, whereas that of the negative gradient sandwich panels is the lowest.

Despite a great deal of research on the sandwich panels with polymer foam core under impact and blast loads, there is no single source available on the blast performance of the metallic sandwich panel with a graded polyurethane foam core that provides complete data on the deformation mechanism and energy absorption capacity of the panels. Thus, in the present study, a series of experiments have been carried out on the sandwich panels with aluminum face sheets and polyurethane foam core with different relative densities of 4%, 8%, and 12%, while the mass, as well as the thickness of the panel, is constant. The polyurethane foam was selected as the core of the panel due to its several advantages such as lower material costs, higher impact damping and resistance, and superior acoustical and thermal insulating



**Fig. 1** A typical sandwich panel with triple-layered polyurethane foam core (The core thickness is 30 mm while the back and front face sheet thicknesses are 1 mm)

**Table 1** Sandwich panel testing groups

| Configuration type | Geometry  | Configuration code | Core layer thickness (mm) |
|--------------------|---|--------------------|---------------------------|
| 1                  |    | P1MT30             | 30                        |
| 2                  |    | P2LHT30            | 15 + 15                   |
|                    |   | P2HLT30            | 15 + 15                   |
| 3                  |  | P3LMHT30           | 10 + 10 + 10              |
|                    |  | P3HMLT30           | 10 + 10 + 10              |

properties. Of interest in this paper is an analysis of the effect of different layering configurations and core thicknesses, and the number of core layers on the response of the panel under the same loading condition. According to the experimental results, corresponding numerical simulations have been performed using ANSYS/Autodyn finite element code. A three-dimensional numerical model is developed for the investigation of the behavior of sandwich panels under

blast loading. The numerical simulation results are investigated from different points of view as the process of the blast and structural response, fluid–structure interaction pressure characteristics, the deformation and velocity response, and the energy absorption capacity. Details of the experimental study and numerical simulations are described in the following sections.

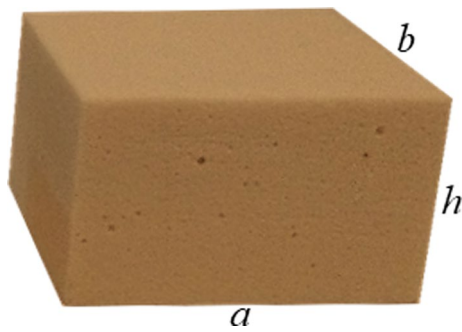


**Fig. 2** Specimens prepared for quasi-static compression tests ( $a=80$  mm,  $b=70$  mm,  $h=50$  mm)

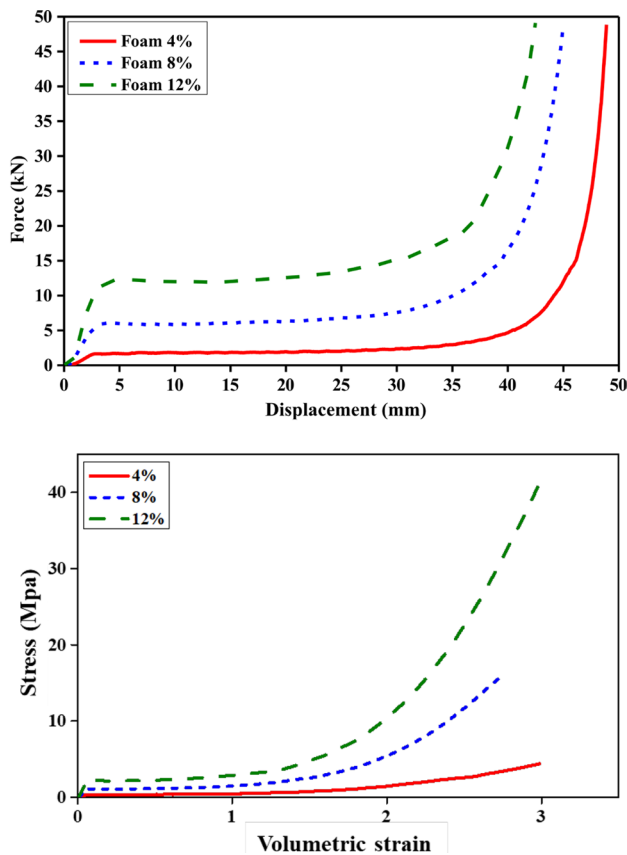


**Fig. 3** Behaviors of polyurethane foams with different density ratios: **a** Quasi-static response; **b** stress–strain curve

## 2 Experimental procedure

### 2.1 Material and specimen

The sandwich structure used in the present study consists of two metallic face sheets made from Al-6061-T6 aluminum alloy and a core of polyurethane foam with closed cells. The flexible polyurethane foam was synthesized by the rapid



**Fig. 4** Explosive shock tube apparatus

reaction of methylene diphenyl diisocyanate (MDI) and polyether polyol under ambient temperature. It should be mentioned that all foam cores have the same base polyurethane chemistry, and foam cores with the same density were cut from a single piece. The structures were designed and fabricated at the Imam Hossein University at ambient temperature. The core and the face sheets were bonded together using epoxy resin and cured for about 48 h at room temperature. The overall dimensions for the back face sheets were 250 mm long, 250 mm wide, and 1 mm thick, while the front face sheets and core were cut into circular samples with a radius of 77 mm. The thicknesses of the front face sheet and the core height were 1 mm and 30 mm, respectively. In this series of experiments, the total mass and thickness of the panel were constant. An actual sandwich panel specimen with a triple-layered polyurethane foam core is shown in Fig. 1.

As listed in Table 1, three types of sandwich panels with different layering configurations for the core were considered and different relative densities of 4% ( $50 \text{ kg/m}^3$ ), 8% ( $100 \text{ kg/m}^3$ ), and 12% ( $150 \text{ kg/m}^3$ ) were utilized. The letters used in the configuration code column represent the materials, number core of layers, and thickness: P stands for polyurethane foam core, while the number after P is the number of core layers; H stands for high-density core, L stands for low-density core, M stands for middle-density core, and T stands for the height of the panel. For instance, the P3HMLT30 configuration has a 30-mm-thick triple-layered polyurethane foam core with different core densities of high, middle, and low in descending order from the blast side (see Table 1).

Configuration 1 consisted of a single-layered polyurethane core with an average density ratio and height of 8%



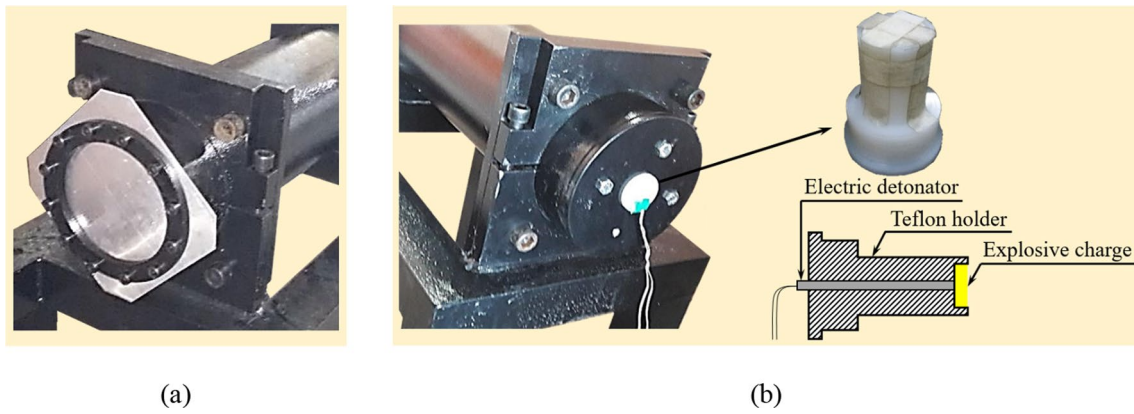


**Fig. 5** Experimental setup: **a** The mounting of the sandwich panel specimen at the front face of the tube; **b** The explosive charge and electric detonator located at the end of the tube using the Teflon holder

**Fig. 6** Clamping arrangement and loading for blast tests: **a** the geometry of sandwich panel specimen; **b** back clamping frame

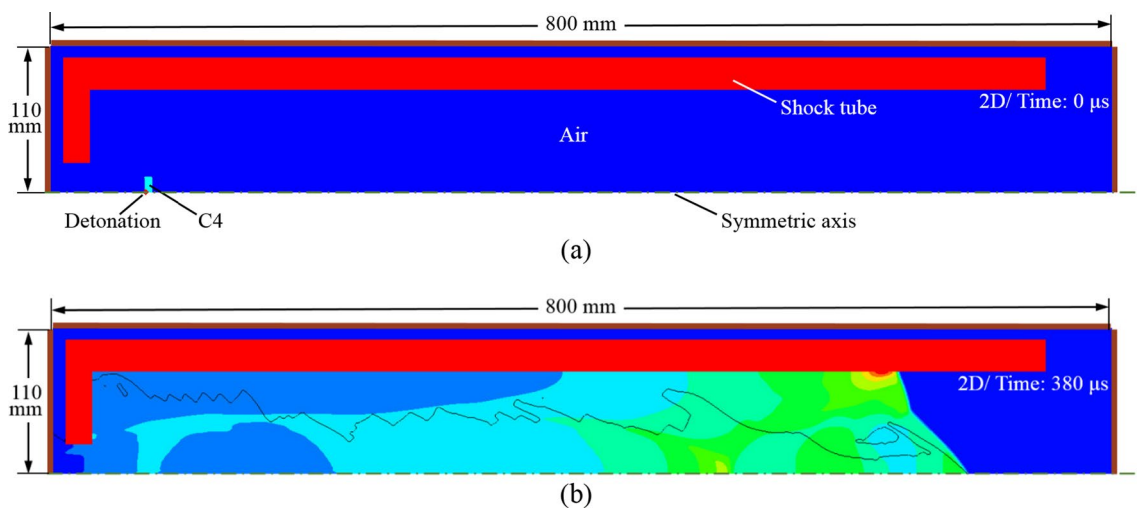
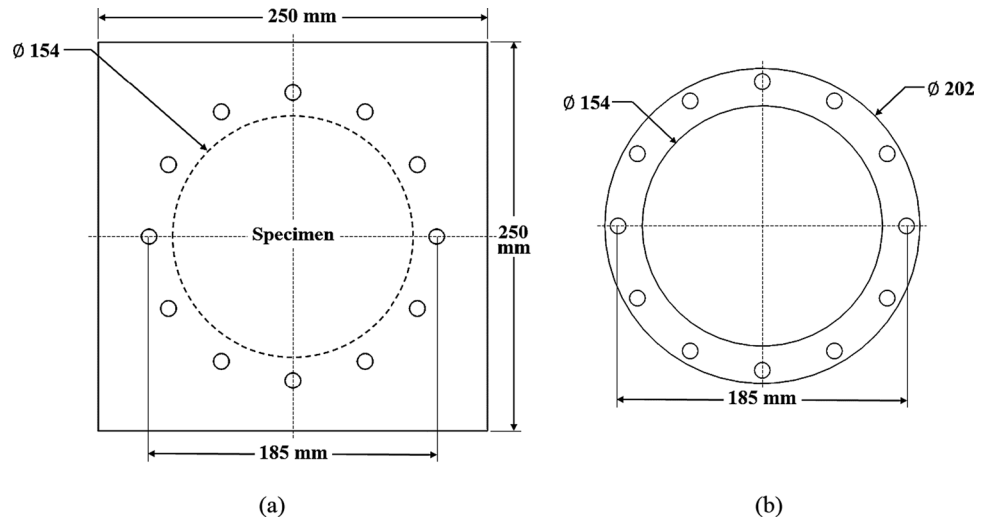


**Fig. 7** Two-dimensional finite element model for blast wave calculation: **a** initial state of the 2D model; **b** pressure contour of the 2D model before remapping

and 30 mm, respectively. Configuration 2 was comprised of a double-layered core where each layer's height was 15 mm. Configuration 3 consisted of a triple-layered core where each layer's height was 10 mm. The average density ratios of configurations 2 and 3 were 8% as well. It should be noted that in the second and third arrangements, the back and front face sheets swapped their positions. It is noteworthy to mention that in these configurations, the first core layer was the one first subjected to the blast load.

To measure the compressive properties of polyurethane foam core for different density ratios, several quasi-static compression tests were carried out at a speed testing of  $3 \text{ mm min}^{-1}$  by using a SANTAM testing machine (Model STM-150) according to the ASTM D1621-00 standard. The specimens were cut into a size of  $80 \text{ mm} \times 70 \text{ mm} \times 50 \text{ mm}$  as shown in Fig. 2.

The quasi-static load was applied until the polyurethane foams with a relative density of 4%, 8%, and 12% were compressed to nearly 2.2%, 10%, and 15% of their original thickness, respectively. Four replicates per specimen were tested, and the results were averaged. Figure 3 represents the quasi-static behavior and stress–strain curve of polyurethane foams with different density ratios.

As shown in Fig. 3, the engineering stress–strain curves obtained from compression tests exhibited three deformation regions of the linear elastic region, plateau stress region, and densification region for all experiments. A large strain range was observed in the plateau stress region, which confirmed the high energy absorption ability of polyurethane foam cores against low-stress levels. The quasi-static behavior had also a clear trend for different core density ratios in which in comparison with the high- and middle-density foams, the lower-density foam had a lower stiffness and strength, as well as a larger strain range for the plateau stress region. Thus, the polyurethane foams exhibited great potential in being employed as core materials in sandwich panels against extreme dynamic loading such as blast load.

## 2.2 Experimental setup

In this series of experiments, an explosive shock tube apparatus was employed to conduct the blast tests as shown in Fig. 4. The apparatus consisted of an explosion chamber made of Steel 4340 with 720 mm length, 77.5 mm inner radius, 101.5 mm outer radius, and 24 mm thickness.

The panel and the steel frame were attached to the front face of the tube with twelve M12 bolts as shown in Fig. 5a. The explosive charge (C4) with a mass of 4 g was molded into a 12-mm-radius flat cylindrical disc and placed at the end of the tube with a constant distance of 676 mm. The charge was detonated via a 0.6 g leader of explosive centrally attached to a detonator. For each test, a Teflon holder was used as shown in Fig. 5b. The clamping arrangements and loading are shown in Fig. 6.

As shown in Fig. 6, the back face sheet was secured between the frame and tube with fully clamped boundary conditions where the core and front face sheets were placed within the tube. Therefore, the dashed line in Fig. 6a shows the core and front face sheets.

## 3 The methodology of numerical simulations

Due to the expansion of computational mechanics methods and computer technology, numerical simulation in finite element commercial software has become a practical tool to assess the physical response of a structure, which leads to accurate design. In this paper, numerical simulations of the conducted experiments were carried out by a commercial code ANSYS/Autodyn using a coupled Eulerian and Lagrangian solver approach. The software permits changing degrees of complexity in dealing with the behavior of different structures subjected to extreme dynamic loading. The details of the numerical simulations have been provided in the following subsections.

### 3.1 Two-dimensional blast loading

As mentioned in the previous section, for all blast tests, a 4 + 0.6 g disc-shaped explosive charge was used to generate the blast loads. The explosive charge dimensions were greatly smaller than that of the specimens and explosion chamber. To decrease the computation cost related to the initial step of the calculations, the remapping capability existing in Autodyn was used which includes the detonation and development of the explosive charge. For saving computational time as well as providing accurate loading in the explosion chamber, the pressure field within the chamber was expanded by mapping the pressure field obtained from a two-dimensional simulation. The

**Table 2** Air and explosive material parameters for Eulerian models

| Material | $\rho$ (kg/m <sup>3</sup> ) | Det. wave speed (m/s)        | $A$ (GPa)   | $B$ (GPa) | $R_1$ | $R_2$ | $\omega$ | $e$ (MJ/kg) |
|----------|-----------------------------|------------------------------|-------------|-----------|-------|-------|----------|-------------|
| C4 [51]  | 1601                        | 8193                         | 609.77      | 12.95     | 4.5   | 1.4   | 0.25     | 6.057       |
| Air [50] | $\rho$ (kg/m <sup>3</sup> ) | Specific heat ratio $\gamma$ | $e$ (MJ/kg) |           |       |       |          |             |
|          | 1.225                       | 1.4                          | 0.2068      |           |       |       |          |             |

two-dimensional Euler domain was created with a much more refined mesh than the full three-dimensional grid. As shown in Fig. 7, the internal region of the explosion chamber, which comprises the explosive charge and the air, was first modeled by using the two-dimensional multi-material Euler formulation in Autodyn. Due to the cylindrical shape of the explosive charge, the two-dimensional axial symmetry condition was utilized until the blast waves interfaced with the explosion chamber. In the numerical simulation, the internal region of the chamber was modeled with 0.25 mm×0.25 mm elements that led to the creation of 1,408,000 Euler multi-material simulation elements. The initiation point of the explosive charge was modeled as shown in Fig. 7, which meets the conducted experiments. The two-dimensional simulation was terminated before the interaction between the explosion chamber and the shockwaves. Next, the pressure field was mapped into the three-dimensional computation domain that comprises the aluminum face sheets and polyurethane foam core. By using the Eulerian solver, the air was modeled in the three-dimensional simulation, which allowed the blast waves to propagate and was fully coupled with the Lagrangian solver. The size of the Eulerian domain was 800 mm×110 mm×110 mm which consisted of the air within the cylindrical explosion chamber and the air circumambient in the exposed area of the sandwich panel.

### 3.2 Material models

#### 3.2.1 Equation-of-state

A general material model needs equations establishing a relationship between stress, internal energy, and deformation. The stress tensor is divided into a stress dilatatory and uniform hydrostatic pressure in most cases. The stress tensor is related to the material's resistance to shear distortion. The relationship between the local specific energy, the local density, and the hydrostatic pressure is introduced as the equation of state. An equation of state expresses the material hydrodynamic response and for the case when the yield stress of the material is less than the hydrodynamic pressure, it can be a preliminary response for solid materials at high rates of deformation. However, performing dynamic experiments is a practical method to

acquire the characteristics of material behavior at high strain rates. In addition to the hydrostatic pressure calculation, defining and considering the relationships between shear strain and stress for a solid material with finite shear strength is essential. Relationships for the definition of the elastic-to-plastic transition behavior, both in release and compression, and also a relationship to introduce the onset of fracture are needed. The yield stress criterion is a function of the strain rate, strain degree, and the temperature of deformation or only involves constant yield stress.

In this paper, the C4 material model existing in the Autodyn material library was utilized to model the C4 explosive charges used in all experiments. To describe the explosive material in the numerical simulations, the Jones–Wilkins–Lee (JWL) equation of state was implemented, which is expressed as [49]

$$p = A \left( 1 - \frac{\omega \rho}{R_1 \rho_0} \right) e^{-\frac{R_1 \rho_0}{\rho}} + B \left( 1 - \frac{\omega \rho}{R_2 \rho_0} \right) e^{-\frac{R_2 \rho_0}{\rho}} + \omega \rho e \tag{1}$$

where  $A$ ,  $B$ ,  $R_1$ , and  $R_2$  are standard constants. Also,  $\omega$  and  $e$  are the specific heat and internal energy, respectively.  $\rho$  and  $\rho_0$  are the density and reference density, respectively.

Furthermore, the ideal gas equation-of-state was used to model the air, which is defined as [50]

$$p = (\gamma - 1)\rho e \tag{2}$$

where  $\gamma$  is the adiabatic exponent. The air and explosive material constants for the Eulerian models are given in Table 2 [50, 51].

To express the hydrodynamic response of the aluminum face sheets, the polyurethane foam core, and the explosion chamber made of steel 4340, a linear shock equation-of-state was used. This equation-of-state is only employed for solid bodies. In the majority of dynamic experiments carrying out measurements of shock velocity ( $U$ ) and particle velocity ( $u_p$ ), it has been obtained that there is a linear empirical relation between the two mentioned parameters for many liquids and most solids over a broad range of pressure. This relation is expressed in the following form [52]

$$U = c_0 + s u_p \tag{3}$$

where  $s$  and  $c_0$  are the linear Hugoniot slope coefficient and bulk sound velocity, respectively.

The most prevalent form of the Mie–Grüneisen equation-of-state that prepares the relation between internal energy and pressure with reference to the shock Rankine–Hugoniot equations is expressed in the following form [52]

$$p - p_H = \Gamma \rho (e - e_H) \tag{4}$$

where  $e_H$  and  $p_H$  are the Hugoniot specific energy as well as pressure. These parameters are only functions of density. By assuming the Grüneisen coefficient ( $\Gamma$ ) as  $\Gamma \rho = \Gamma_0 \rho_0$ , the

**Table 3** Shock equation-of-state parameters for Al 6061-T6 and AISI 4340 steel

| Property       | Al 6061-T6 [53] | AISI 4340 steel [54] |
|----------------|-----------------|----------------------|
| $G$ (GPa)      | 26              | 76.90                |
| $c_0$ (m/s)    | 5240            | 4578                 |
| $s$            | 1.40            | 1.33                 |
| $\Gamma$       | 1.97            | 1.67                 |
| $C_v$ (J/kg K) | 885             | 460                  |



**Table 4** J-C material parameters for Al 6061-T6 and AISI 4340 steel

| Material properties               | Notations                   | Al 6061-T6 [53] | AISI 4340 steel [59] |
|-----------------------------------|-----------------------------|-----------------|----------------------|
| Modulus of elasticity             | $E$ (GPa)                   | 68.9            | 205                  |
| Poisson’s ratio                   | $\nu$                       | 0.33            | 0.3                  |
| Density                           | $\rho$ (kg/m <sup>3</sup> ) | 2700            | 7850                 |
| Yield stress and strain hardening | $A$ (MPa)                   | 324.1           | 792                  |
|                                   | $B$ (MPa)                   | 113.8           | 510                  |
|                                   | $n$                         | 0.42            | 0.26                 |
| Strain rate hardening             | $\dot{\epsilon}_0$ (1/s)    | 1               | 1                    |
|                                   | $C$                         | 0.002           | 0.014                |
| Temperature softening             | $T_0$ (K)                   | 293.2           | 293.2                |
|                                   | $T_{\text{melt}}$ (K)       | 925             | 1793                 |
|                                   | $m$                         | 1.34            | 1.03                 |
| Specific heat                     | $C_p$ (J/kgK)               | 896             | 477                  |
| Fracture strain constant          | $D_1$                       | -0.77           | 0.05                 |
|                                   | $D_2$                       | 1.45            | 3.44                 |
|                                   | $D_3$                       | 0.47            | -2.12                |
|                                   | $D_4$                       | 0               | 0.002                |
|                                   | $D_5$                       | 1.6             | 0.61                 |

Hugoniot pressure, as well as specific energy, are defined as Eqs. (5) and (6), respectively, from fitting experimental data. The Gruneisen coefficient is mostly approximated  $\Gamma \sim 2s - 1$  in the literature.

$$p_H = \frac{\rho_0 c_0^2 \eta (\eta - 1)}{[\eta - s(\eta - 1)]^2} \tag{5}$$

$$e_H = \frac{1}{2} \frac{p_H}{\rho_0} \left( \frac{\eta - 1}{\eta} \right) \tag{6}$$

where

$$\eta = \frac{\rho}{\rho_0} \tag{7}$$

In the above equation,  $\Gamma_0$  is Gruneisen’s gamma at the reference state. By eliminating  $\Gamma$  and  $e_H$  from the above equations, the following relation is obtained.

$$p = \frac{\rho_0 c_0^2 (\eta - 1) \left( \eta - \frac{\Gamma_0}{2} (\eta - 1) \right)}{[\eta - s(\eta - 1)]^2} + (\Gamma_0 \rho_0 e) \tag{8}$$

where  $\rho_0 c_0^2$  is designated as the elastic bulk modulus at small nominal strains.

It should be mentioned that for  $s > 1$ , as the pressure tends to infinity, a limiting value of the compression is given by the above formulation. The denominator of the equation-of-state presented in Eq. (8) becomes zero. Therefore, the pressure becomes infinite for  $\eta - s(\eta - 1) = 0$ , which gives the maximum density of  $\rho = \rho_0 s / (s - 1)$ . At this limit, there

is a tensile minimum; afterward, negative sound velocities are computed for the material. It is worth mentioning that the assumption of constant  $\Gamma \rho$  is likely not reliable, long before this regime is approached. Moreover, the assumption of linear variation between the particle velocity ( $u_p$ ) and shock velocity ( $U$ ) does not hold for a large compression.

The linear  $U - u_p$  equation-of-state was implemented in ANSYS/Autodyn, and the values of three variables,  $c_0$ ,  $s$ , and  $\Gamma$  were considered as Table 3 for its full definition [53, 54].

### 3.2.2 The crushable foam strength model

To describe the polyurethane foam behavior, a linear equation-of-state, as well as a crushable foam strength model, was used. The crushable foam strength model is a comparatively straightforward model designed to demonstrate the crush specifications of foam materials subjected to a non-cyclic load such as blast loading conditions. The dependence of the strain rate of the foam material was included in the model by defining the dynamic increase coefficient (DIF) 2. According to previous studies [55, 56], in compressive stress–strain curves of PU foams, the stress values under quasi-static conditions are approximately 50% of the corresponding dynamic values. The rate dependency of the PU foam stems from two facts: (a) the strain-rate dependency of the solid PU of the cell walls and (b) the compressibility of the air trapped in the closed cells. In the crushable foam, the behavior of principal stress versus volumetric strain is the same as in Fig. 3. This model should be employed with isotropic elasticity

and incremental elastic update of pressure as the following equation and stress deviators are used [52].

$$P^{n+1} = P^n + K \dot{\epsilon}_v^{n+1/2} \Delta t^{n+1/2} \quad (9)$$

$$S_{ij}^{n+1} = S_{ij}^n + 2G \left( \dot{\epsilon}_{ij}^{n+1/2} - \delta_{ij} \dot{\epsilon}_v^{n+1/2} \right) \Delta t^{n+1/2} \quad (10)$$

where

$$\dot{\epsilon}_v^{n+1/2} = \left( \frac{\dot{V}}{V} \right)^{n+1/2} \quad (11)$$

$\delta_{ij}$  is the Kronecker delta.

For the current volumetric strain, the amounts of the resulting principal stresses and the allowable principal compaction stress are compared with each other. For the case when the principal stress value is greater than the maximum allowable compaction stress, it is decreased to the allowable magnitude. For the case when the tentative principal stress value ( $\sigma_i^{*,n+1}$ ) is greater than the maximum allowable principal compaction stress, it is diminished to this limit. Also, a negative tentative principal stress greater than the maximum is reduced to the negative value of the limit.

$$\text{if } \sigma_i^{*,n+1} \geq \sigma_i^{\text{compaction}}(\epsilon_v) \text{ then } \sigma_i^{n+1} \geq \sigma_i^{\text{compaction}}(\epsilon_v) \frac{\sigma_i^{*,n+1}}{|\sigma_i^{*,n+1}|} \quad (12)$$

To obtain the final stress update, the principal stresses are returned to the global system after scaling them down. It is worth mentioning that the transmission of the principal stresses back to the compaction stress is independently carried out in each principal direction, which shows that the plastic Poisson's ratio is zero.

The behavior of compaction is described as a piecewise linear principal stress versus volumetric strain curve, while the volumetric strain is expressed as the natural logarithm of the volume ratio presented in Eq. (13),

$$\epsilon_v = \ln \left( \frac{V_0}{V} \right) \quad (13)$$

where  $V_0$  and  $V$  are the original volume and the volume after deformation, respectively. The stress–strain behaviors of the polyurethane foams used in the numerical simulations are presented in Fig. 3. Indeed, several quasi-static compression tests were performed in this study to obtain the mechanical behavior of polyurethane foam cores and the deformation rate (speed of testing) of tested specimens

is not appropriate for blast-loaded structures. However, as mentioned in Refs. [55, 57], the quasi-static compressive stress–strain curves of polyurethane foam core possess very similar characteristics to the dynamic curves and the stress level is much lower under quasi-static loading conditions. Chen et al. [55] noted that the strength values of polyurethane foam cores under quasi-static conditions are only ~50% of the corresponding dynamic values. Therefore, in conducted numerical simulations, a correlation factor of 2 was considered for the experimental stress–strain curves of foam cores with different densities. This dynamic increase factor was considered to be constant for all rested numerical simulations and was not changed.

### 3.2.3 Johnson–Cook plasticity model

As mentioned before, in the current study, aluminum plates and the thick-walled steel explosion chamber were considered elastic–plastic materials for finite element simulations. According to the literature, the Johnson–Cook (J-C) thermoplasticity model is a practical model to represent the flow stress behavior of metallic materials against extreme dynamic loads, large strains, and high temperatures. Generally, the material response subjected to blast loading involves consideration of influences of strain, strain rate, and temperature. In the J-C phenomenological plasticity model, the effects of quasi-static yielding, strain hardening, strain-rate hardening, and thermal softening of material are taken into account. Note that the J-C material parameters related to these effects have been archived in a database of ANSYS/Autodyn software. The J-C plasticity model expresses the von Mises flow stress ( $\sigma$ ) as the following equation [58]

$$\sigma = \left( A + B \epsilon_{pl}^n \right) \left( 1 + C \ln \epsilon_{pl}^* \right) \left( 1 - T_H^m \right) \quad (14)$$

where  $A$  is the initial yield stress at low strains,  $B$  and  $n$  are hardening constant and hardening exponent, respectively,  $\epsilon_{pl}$  is the effective plastic strain,  $C$  is the strain rate constant,  $\epsilon_{pl}^*$  is the normalized effective plastic strain rate,  $m$  is the thermal softening exponent, and  $T_H$  is the homologous temperature defined as  $(T - T_{room}) / (T_{melt} - T_{room})$ . It should be mentioned that in Eq. (14), the first bracket defines stress as a function of strain including strain hardening, while the second and third brackets represent the effect of strain rate and thermal softening on the material yield strength. In the third bracket, for the case, while the melting temperature is reached, the yield stress approaches zero. In the present work, the J-C material parameters of both the

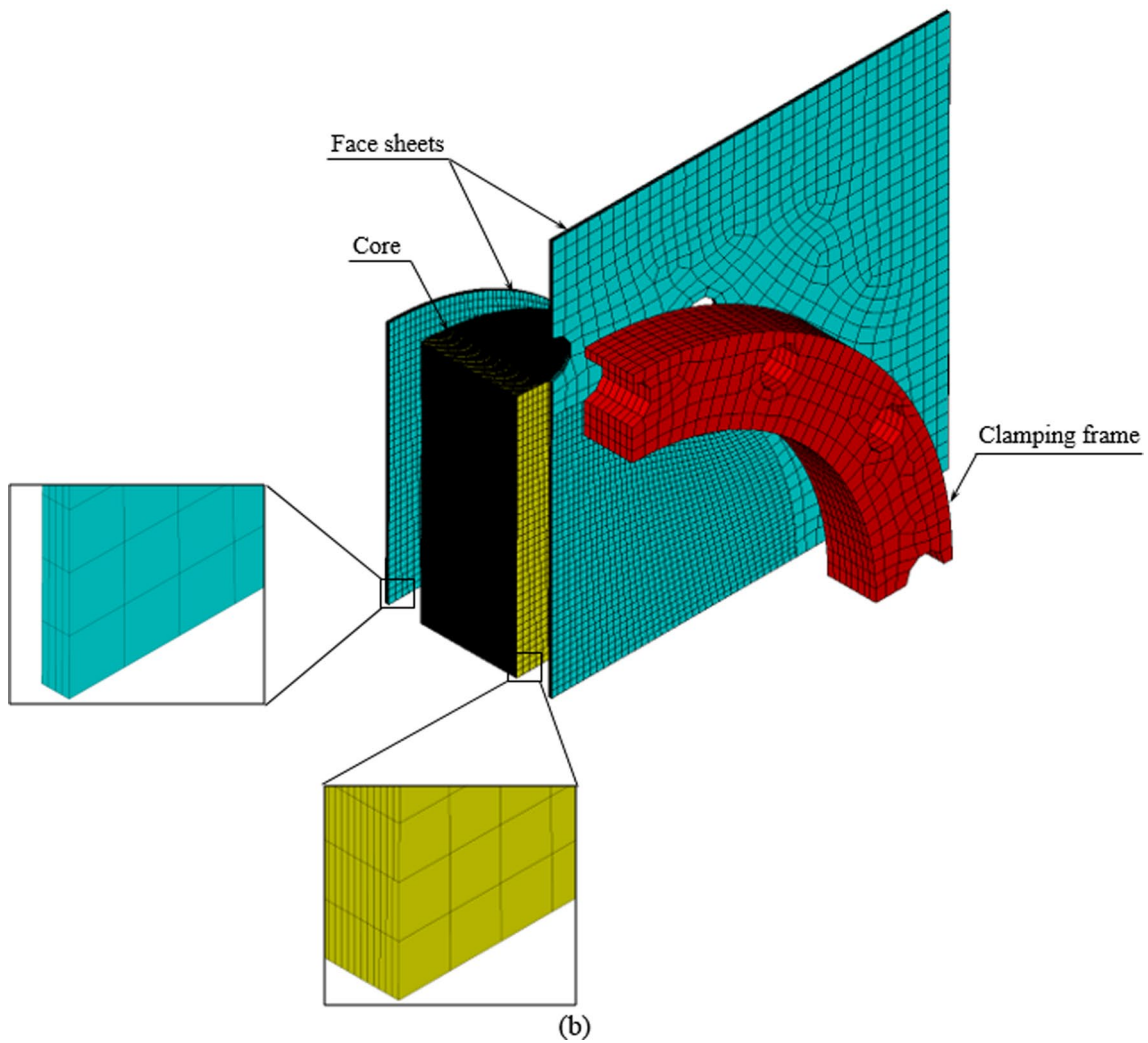
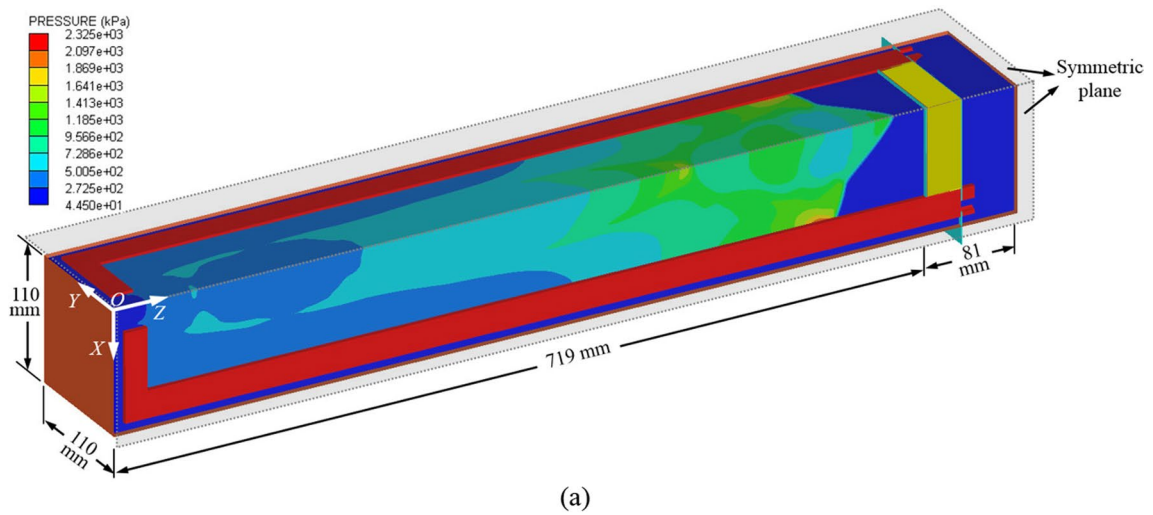


**Fig. 8** Setup for the three-dimensional numerical model: **a** complete assembly; **b** sandwich panel specimen and back clamping frame

explosion chamber (AISI 4340 steel [59]) and aluminum plate (Al 6061-T6 [53]) are depicted in Table 4.

### 3.2.4 Johnson–Cook Failure model

In the current study, for a description of the ductile failure of materials, the J-C failure model is used. The J-C failure model is constructed in an analogous way to the J-C phenomenological plasticity model and it is comprised of three independent terms. This model defines the dynamic fracture strain ( $\epsilon_f$ ) in terms of pressure, strain rate, and temperature as the following equation [58]

$$\epsilon_f = \left( D_1 + D_2 e^{(D_3 \sigma^*)} \right) (1 + D_4 \ln \dot{\epsilon}^*) (1 + D_5 T^*) \quad (15)$$

where  $D_1 - D_5$  are damage parameters,  $\sigma^*$  is the mean stress normalized by the effective stress, and  $\dot{\epsilon}^*$  is the dimensionless strain rate. It should be mentioned that in Eq. (15), the first bracket is the stress dependence, and the second and third brackets are the strain rate dependence and the temperature dependence, respectively. The total damage of the material can be expressed as

$$\epsilon_{eff} = \frac{2}{3} \sqrt{ \left( \epsilon_1^2 + \epsilon_2^2 + \epsilon_3^2 \right) - \left( \epsilon_1 \epsilon_2 + \epsilon_2 \epsilon_3 + \epsilon_1 \epsilon_3 \right) + 3 \left( \epsilon_{12}^2 + \epsilon_{23}^2 + \epsilon_{13}^2 \right) } \quad (17)$$

$$D = \sum \frac{\Delta \epsilon}{\epsilon_f} \quad (16)$$

where  $\Delta \epsilon$  is the incremental effective plastic strain. It is assumed that the material is intact until  $D = 1$  [5, 60, 61]. At this point, the failure of the material in the element is initiated. All of the stresses in the elements, which satisfy this damage, become zero and remain at zero for the specific element.

### 3.2.5 Element erosion

In modeling and solving the Lagrangian FE formulations, element distortion eventuates a major problem. Due

to highly distorted elements, an inaccurate calculation of strains and stresses is obtained. Since the time step depends on the smallest element in the mesh, highly distorted elements result in a large computational time. To counteract this issue, several strategies such as adaptive re-meshing, element erosion, and automatic mass scaling have been developed. In this paper, the element erosion was used [52].

Erosion is an important numerical mechanism that automatically removes or deletes elements from the rest of the mesh during a simulation. The preliminary reason to use erosion is the elimination of highly distorted elements from a simulation before they become degenerate completely. This permits enabling an appropriate and reasonable time step and leads to the continuation of the simulations up to the proper termination time. There are several mechanisms for the initiation of the element erosion such as geometric strain, minimum time step, material failure, and retained inertia. In the present study, the geometric strain limit erosion was employed due to the large deformations that occurred while the nodes were displaced abnormally. The geometric strain is a measurement of an element distortion and can be obtained from the principal strain components as in Refs. [52, 62, 63]

The geometric strain erosion option allows the deletion of elements, while the local element strain becomes greater than a specified value. In this paper, the constant value of 2 was considered as the maximum plastic strain.

### 3.3 Numerical modeling

The blast load was modeled with three-dimensional Euler elements, by remapping the two-dimensional axial symmetry simulation result, consisting of both the surrounding air material properties and C4, into the three-dimensional Euler domain. Figure 8 shows the three-dimensional numerical model, which consists of the aluminum face sheets (turquoise), the polyurethane foam core (yellow), the explosion

**Table 5** Comparison between the experimental and numerical results for the maximum central displacement of the back and front face sheets of the sandwich panel

| Configuration code | Maximum central displacement (mm) |            |                   |            | Deviation % |      |
|--------------------|-----------------------------------|------------|-------------------|------------|-------------|------|
|                    | Experimental results              |            | Numerical results |            | Front       | Back |
|                    | $\delta_f$                        | $\delta_b$ | $\delta_f$        | $\delta_b$ |             |      |
| P1MT30             | 28.2                              | 17.0       | 29.0              | 15.6       | 2.8         | 8.2  |
| P2LHT30            | 30.7                              | 17.5       | 33.5              | 18.0       | 9.1         | 2.8  |
| P2HLT30            | 23.0                              | 13.5       | 24.2              | 14.3       | 5.2         | 5.9  |
| P3LMHT30           | 32.7                              | 18.0       | 34.4              | 19.5       | 5.2         | 8.3  |
| P3HMLT30           | 20.6                              | 11.5       | 21.3              | 13.0       | 3.4         | 13.0 |

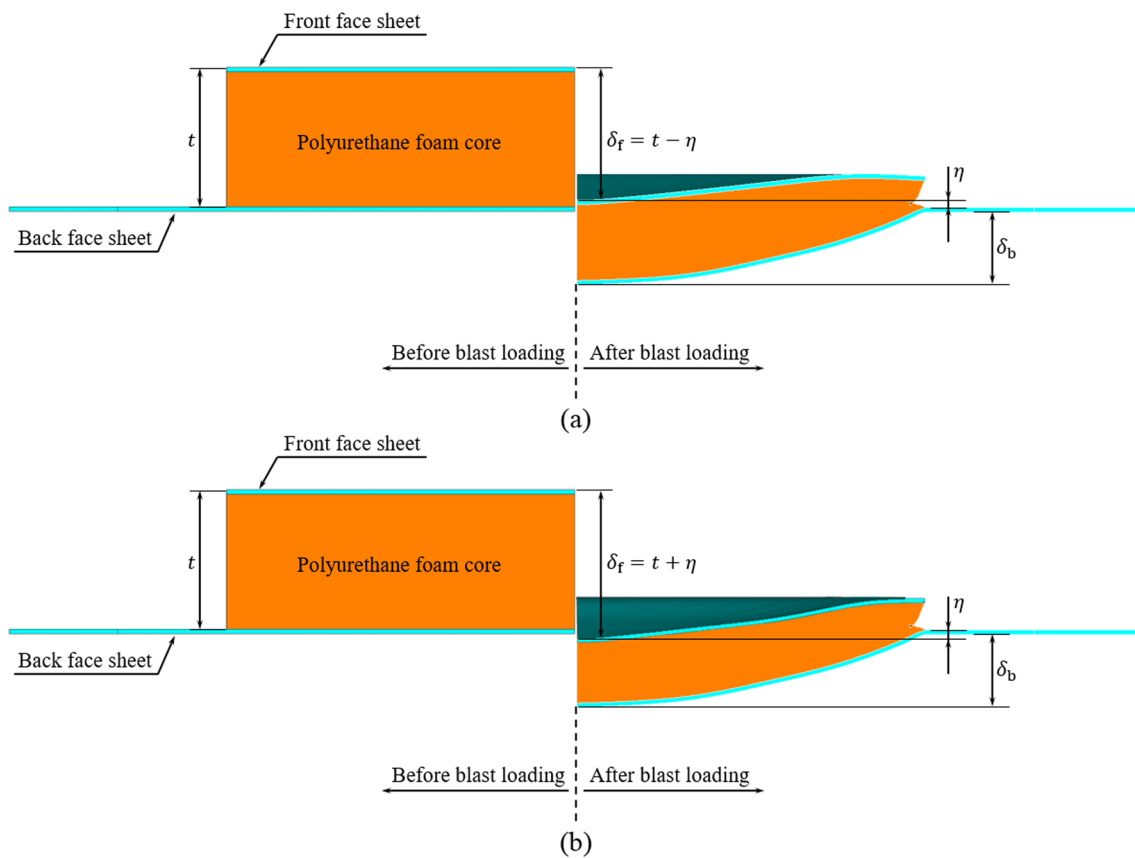


**Fig. 9** Numerical crosscut deformation profiles of P1MT30 configuration before and after blast loading ( $\delta_f$  and  $\delta_b$  are the maximum central displacement of front and back face sheets, respectively)

chamber (red), the clamping frame (red), and the Euler domain elements containing the surrounding air (dark blue) and the remapped properties of 4 + 0.6 g explosive charge 0.38 ms after detonation (pressure contour). One-quarter of the test setup was modeled to decrease computational costs. In all models, the Euler element size was considered as 1 mm × 1 mm × 1 mm, while the simulation time duration was 2 ms.

Interactions between the Lagrangian and Euler elements were defined by using the “fully automatic” Euler–Lagrange Coupling option existing in ANSYS/Autodyn. The flow-out boundary conditions were assigned to all finite sides of the Euler domain (To prevent the influences of detonation reflections during the propagation process), except on the upper and lower surfaces of the explosion chamber as this was a reflective boundary.

Both the face sheets and the core were meshed by three-dimensional eight-noded solid elements. It should be mentioned that in the full three-dimensional model, the back face sheet was divided into two different zones determined by the mesh geometry. The first zone of the back face sheet consisted of a circular exposed area with a radius of 77 mm. The element size in this zone is 2 mm × 2 mm × 0.25 mm

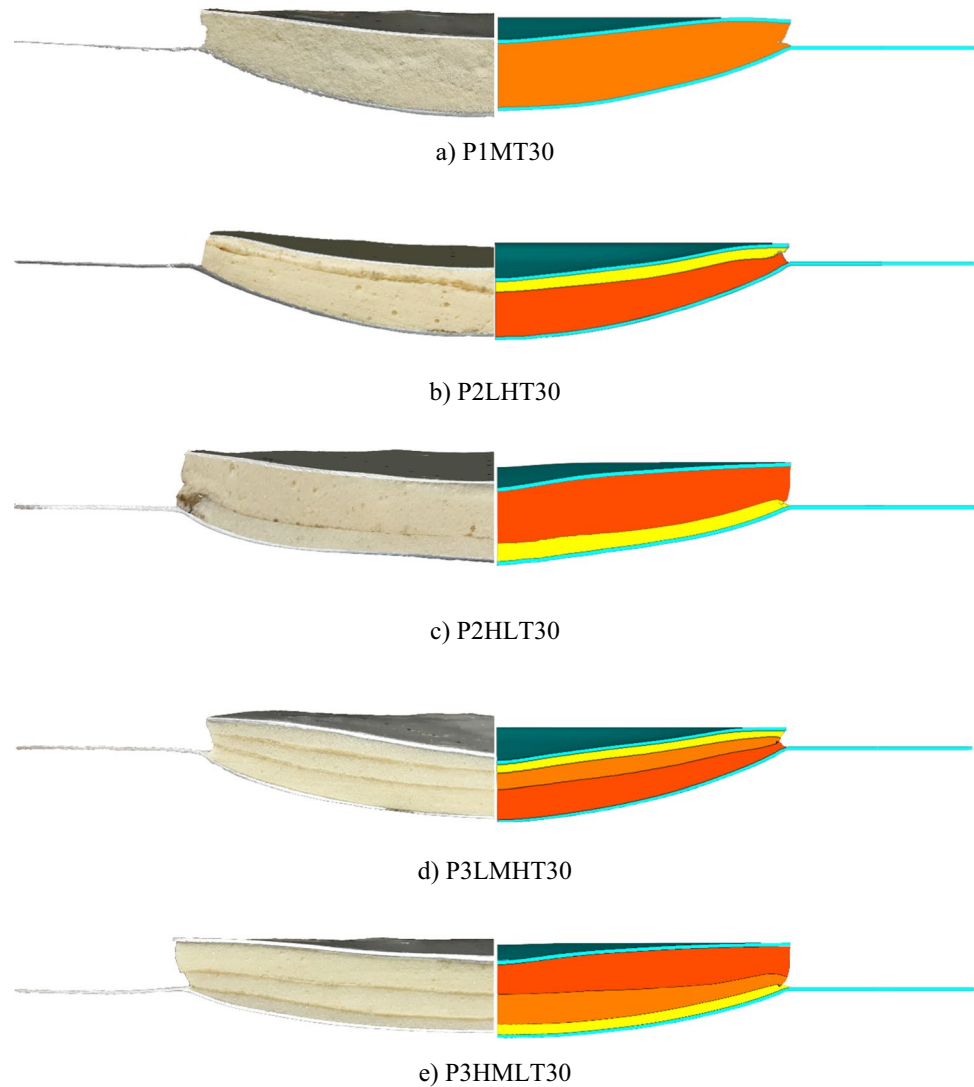
in side. The second zone of the back face sheet consisted of the region under the clamping frame so that the element size in this zone is 4 mm × 4 mm × 0.25 mm. Note that the mesh geometry of the front face sheet is the same as the first zone of the back face sheet, while the element size in the polyurethane foam core side is 2 mm × 2 mm × 0.25 mm. For providing a precise demonstration of the experimental restraints, the steel clamping frame that was employed to support the back face sheet is included in the model. The clamping frame was modeled and its mesh geometry is the same as the second zone of the back face sheet. It should be noted that free boundary conditions were assigned to the front face sheet and the core. Perfect jointing between the face sheets and polyurethane foam core was assumed.

### 3.4 Numerical prediction of structural deformation

For calibration of the material parameters used in the J-C plasticity and failure model, boundary conditions, and Euler–Lagrange coupling in numerical simulations, predicted results are contrasted to those obtained from the conducted experiments in terms of maximum permanent central displacements of face sheets and crosscut



**Fig. 10** Photographs and numerical predictions of crosscut deformation profiles of sandwich panels with different configurations: **a** P1MT30; **b** P2LHT30; **c** P2HLT30; **d** P3LMHT30; **e** P3HMLT30



deformation profiles of sandwich panels. Five different configurations of the present experimental study were used to validate the proposed numerical model. It should be mentioned that to inspect the deformation profiles of the sandwich panels at the center, the tested panels were cut by a water jet along the mid-plane.

The measured maximum central displacement of both the front face sheets and back face sheets and the corresponding simulations are documented and compared in Table 5. It should be noted that for both the front and back face sheets, the predicted displacements by numerical simulations were considered as the average out-of-plane displacement of the central nodes. Figure 9 shows clearly how the front and back face sheet displacements were measured. According to this figure, the displacement of the center of the front and back face sheet relative to the clamped edges of the back face sheet is measured. The displacements were measured using a caliper. The effect of

structural support provided by the polyurethane foam core was enfeebled so that at the same time, the front face sheet experienced larger plastic deformation while the back face sheet underwent lower plastic deformation due to the less acting force transmitted by the polyurethane foam core. The results documented in the deviation column show that for all cases except the back face sheet of the P3HMLT30 configuration, the numerical simulations over-predicted the maximum central displacements of both the front and back face sheets by less than 10%. Apart from that, it can be concluded that the numerical simulation results are consistent with conducted experiments for all configurations according to the complex nature of blast loading and sandwich panels.

To check the correlation between the numerical and experimental results in terms of deformation modes, the crosscut deformation profiles for all sandwich panels with different configurations obtained from numerical

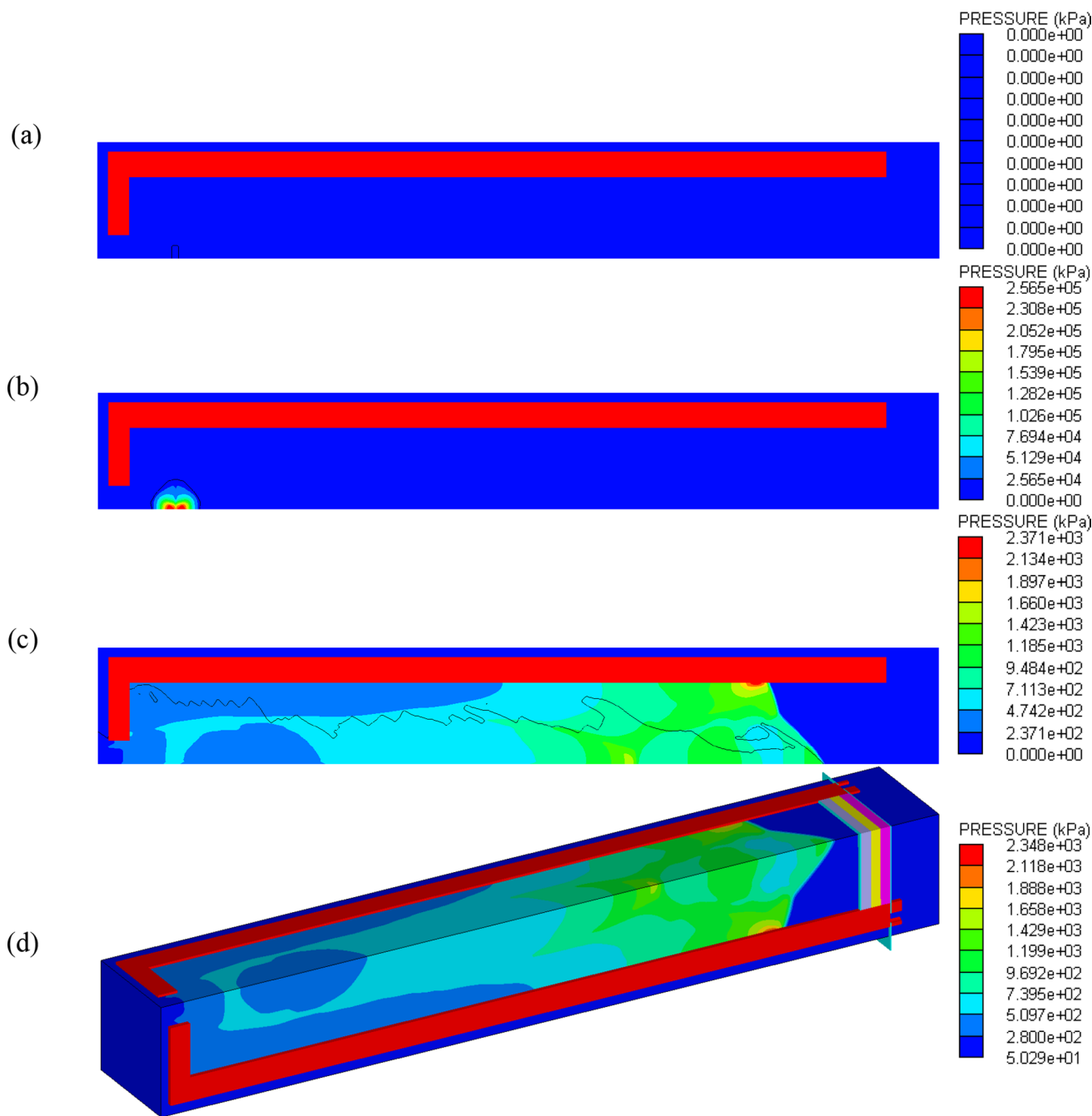


**Fig. 11** Typical processes of the charge detonation, explosion product–structure interaction, and sandwich panel deformation: **a**  $t = 0 \mu\text{s}$ ; **b**  $t = 5 \mu\text{s}$ ; **c**  $t = 380 \mu\text{s}$ ; **d**  $t = 384 \mu\text{s}$ ; **e**  $t = 404 \mu\text{s}$ ; **f**  $t = 414 \mu\text{s}$ ; **g**  $t = 507 \mu\text{s}$ ; **h**  $t = 527 \mu\text{s}$ ; **i**  $t = 770 \mu\text{s}$ ; **j**  $t = 1045 \mu\text{s}$ ; **k**  $t = 2000 \mu\text{s}$

simulations were compared to the experiments and are illustrated in Fig. 10. The right-handed side of this figure is the results of numerical simulations, whereas the left-handed side contains the crosscut deformation profile obtained from experiments. As shown in Fig. 10, the residual deformation modes were analogous between the numerical and experimental results, and in general form, the numerical simulation captured the measured

deformation profile of the sandwich panels for all configurations under blast loading. Therefore, it can be concluded that the predictability of the numerical model is reliable and the current model can accurately demonstrate the deformation profile of the structure, while the time step is close to the maximum displacement. Albeit, there is a visible discrepancy at this point, with the numerical modeling predicting a higher deformation than is observed

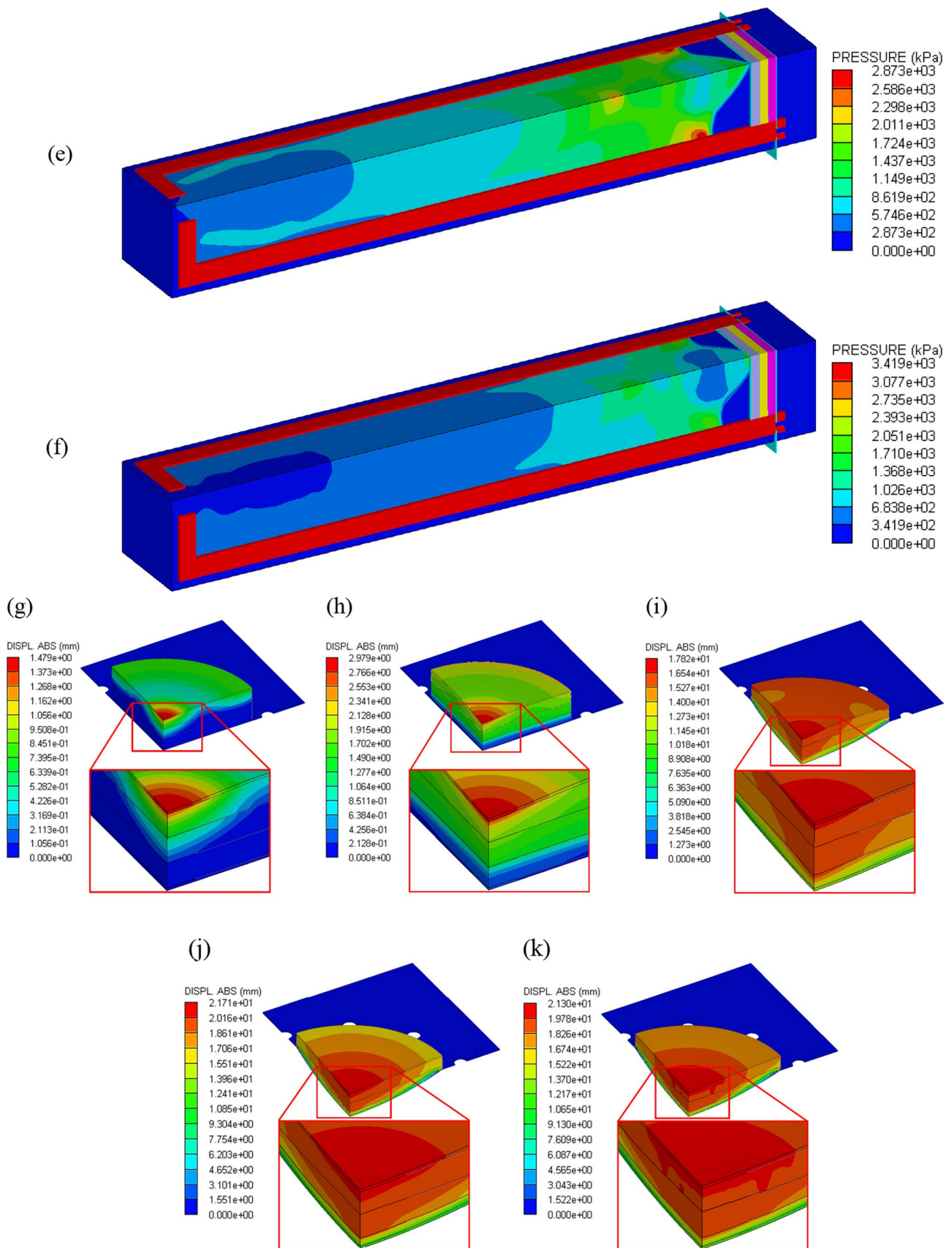
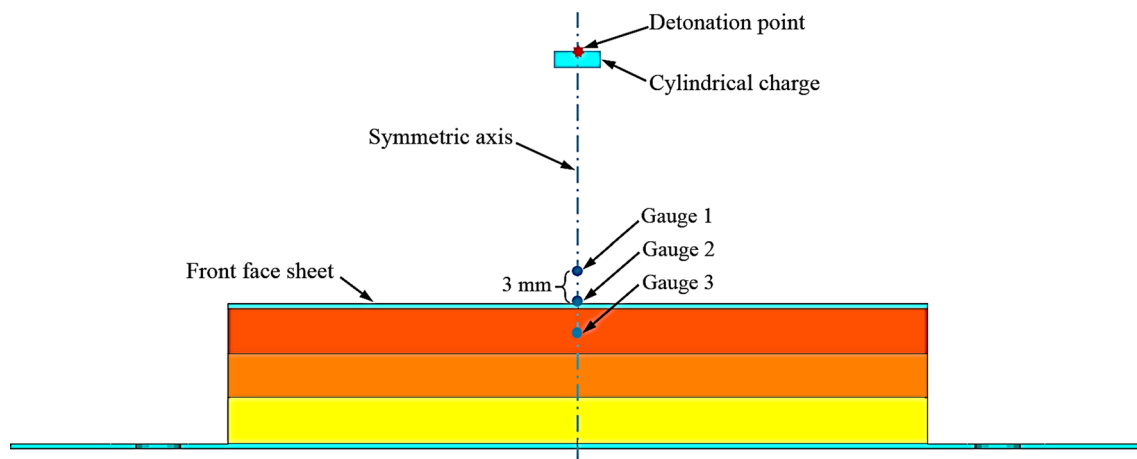


Fig. 11 (continued)



**Fig. 12** A schematic illustrating the locations of juxtaposed pressure gauges with the same distance

in the experiment, whereas no failure was captured in the numerical simulations.

## 4 Results and discussion

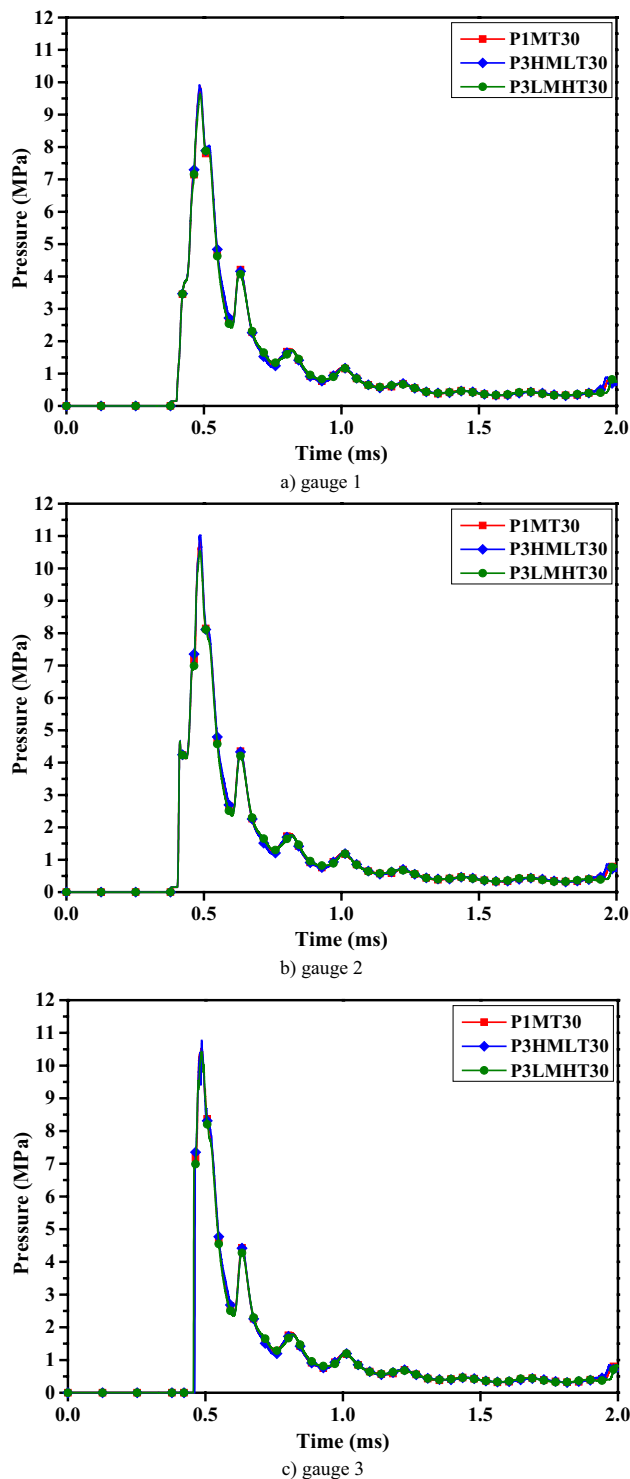
In this section, the numerical simulation results of the present sandwich panels subjected to blast loading are investigated from four points of view: 1) blast and structural response; 2) fluid–structure interaction (FSI) pressure distributions; 3) deformation pattern and velocity response; 4) energy absorption capacity. Each aspect is individually explained in the subsequent subsections.

### 4.1 Blast and structural response

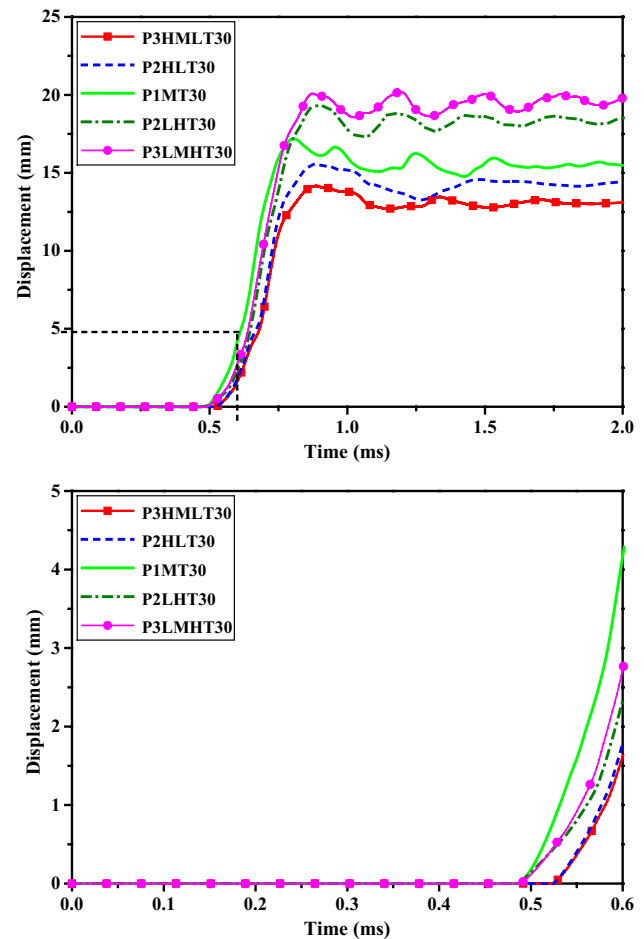
Reviewing the literature shows that the dynamic response of sandwich panels subjected to impulsive loading is split into three different successive phases: FSI phase, core compression phase, and dynamic structural response phase.

Figure 11 represents a typical process of charge detonation, explosion product–structure interaction, and consequent sandwich panel response, which was calculated by the finite element numerical model. The presented model describes the P3HMLT30 configuration. As aforementioned, in the two-dimensional blast loading section, the processes of the charge detonation and initial propagation of detonation waves were simulated in a two-dimensional axial symmetry model. Figure 11a shows the initial state of the two-dimensional model. In Fig. 11b, the C4 explosive charge is detonated and a shock wave is then produced, which leads to an increase in the explosive temperature at the detonation point and also the initiation of a chemical reaction within a small zone just behind the wave. This small zone is called the reaction zone.

In Fig. 11c, an impedance mismatch occurs and the shock wave is transferred at lower pressure through the boundary, for the case, while the shock wave reached the boundary of the charge material and the surrounding air. Figure 11d shows the initial state of the three-dimensional model, after remapping the final state of the two-dimensional model to that. Figure 11e shows the expansion of explosive volume so that the produced shock wave first impacts the front face sheet of the sandwich panel at the center. From this time onward, the interaction between the front face sheet and the explosive product commenced. The interaction takes place over a time duration of almost 10 ms until the contact force between the front face sheet and explosive approximately diminishes to 0. Figure 11f shows the FSI stage, where the front face sheet has obtained an initial velocity due to the effect of the shock wave on the plate. At this moment, the velocity of the core and the back face sheet is zero. This figure also depicts the backward distortion of explosion products due to the reflection from the front face sheet. In Fig. 11g, the polyurethane foam core starts to compress successively and the densification of the polyurethane foam core gradually occurs due to the high compression velocity of the front face sheet, as shown in Fig. 11h. At this moment, the back face sheet velocity is zero. The core compression reduces from the central to the peripheral region. In Fig. 11i, the front face sheet is decelerated by the polyurethane foam core, while the back face sheet and the core are accelerated. In this stage, the structure obtains the same velocity and goes into a new phase, called the dynamic structural response. In this phase, the structure deforms under its inertia and its deformation extends towards and backward with the momentum transmission, as shown in Fig. 11j. Eventually, the structure is brought to rest by the dissipation of the kinetic energy due to the plastic bending and stretching, as shown in Fig. 11k.



**Fig. 13** Pressure–time histories of gauges obtained from numerical simulations for different configurations: **a** gauge 1; **b** gauge 2; **c** gauge 3



**Fig. 14** Displacement–time history of the back face sheets for all panels at the center point (enlarged review of 0–600  $\mu$ s)

## 4.2 FSI pressure distribution

In the current experimental study, the pressure–time history during the detonation of the explosive charge was not recorded. Therefore, the effect of graded polyurethane foam core on FSI pressure distributions was numerically studied. For this, three successive pressure gauges with a constant distance of 3 mm were considered along the axis of the cylindrical explosion chamber to trace the pressure distribution in the vicinity of the FSI surface. Figure 12 illustrates the locations of the pressure gauges so that the transmitted shock wave profile is firstly recorded by gauge 1, the pressure of the reflected wave on the top surface of the sandwich panel is recorded by gauge 2, the effect of graded foam core as well as the number of core layers on pressure distribution is recorded by gauge 3 located on the left-hand side of the undeformed front face sheet. The pressure–time histories of three configurations, P1MT30, P3HMLT30, and P3LMHT30 are compared to assess the influence of graded foam core and the number of core layers on the FSI



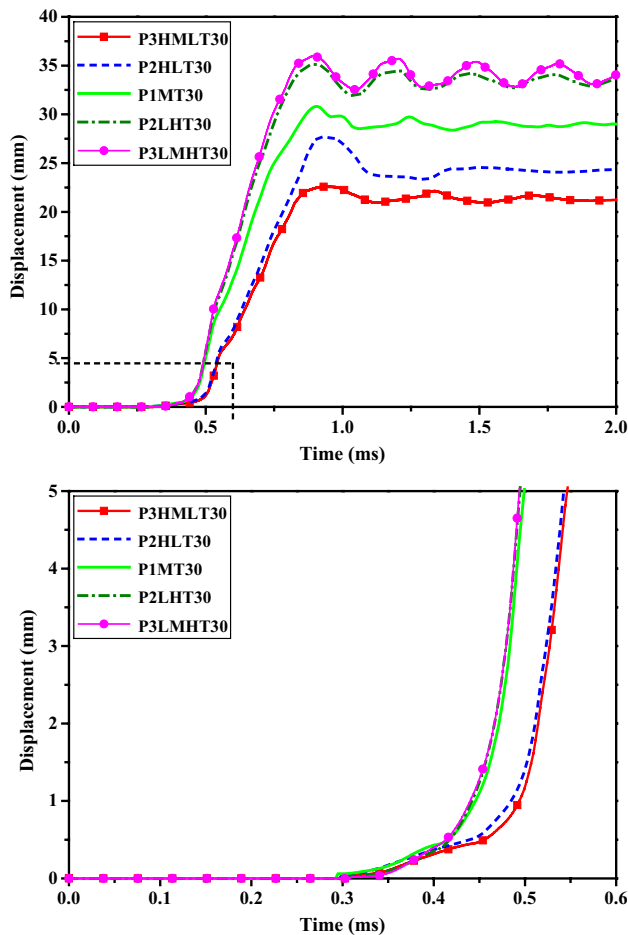


**Fig. 15** Displacement–time history of the front face sheets for all panels at the center point (enlarged review of 0–600  $\mu$ s)

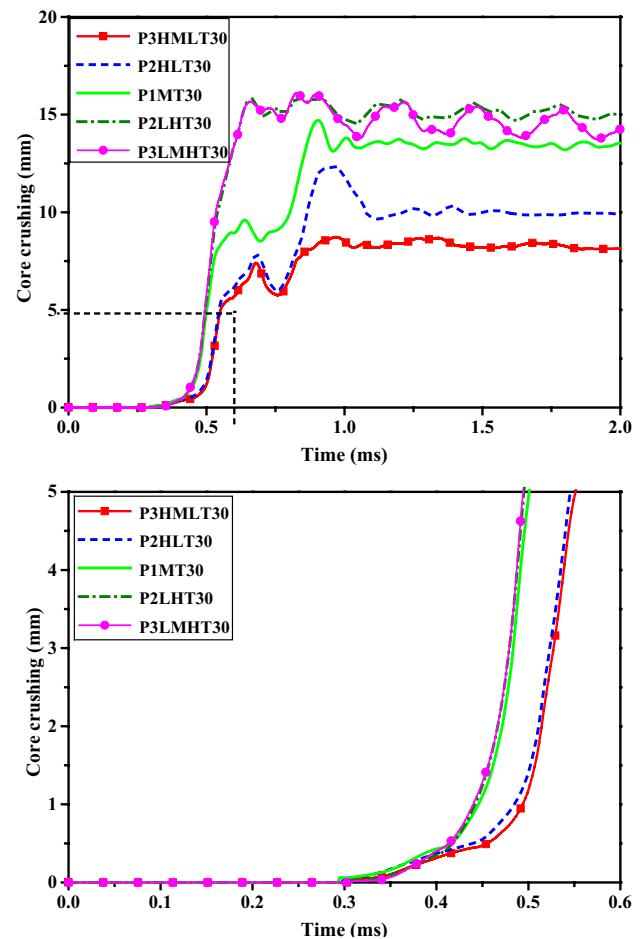


**Fig. 16** Displacement–time history of the core for all panels at the center point (enlarged review of 0–600  $\mu$ s)

pressure distributions. The pressure–time histories obtained from numerical simulations are represented in Fig. 13 for the above configurations.

It is apparent that the pressure–time histories recorded by the same gauges overlap for different configurations. The propagation of the shock wave is directly related to the stiffness of the obstacle structure. As a consequence, the graded foam core strategy did not influence the interaction between the front face sheet and shock wave, because the compressive modulus of polyurethane foam is here less than that of the aluminum face sheet by three orders of magnitude. It should be mentioned that due to shock wave reflection, a double-humped characteristic is observed from the pressure–time curves recorded above the front face sheet. This characteristic is commonly determined by a low and a high jump for incident shock wave and reflected shock wave, respectively. An incident shock wave is produced when the atmosphere around the explosion is intensely compressed by gases generated by the chemical reaction of explosives. A closer look on Fig. 13 shows that the pressure

jump phenomenon is not conspicuous, particularly for the low jump. This could be probably due to the nonlinear compressibility influence of air medium that generates a real enhancement in the amounts of the stagnation pressure experienced by air particles upon blast arrival. While the shock wave confronted the top surface of the front face sheet, the shock wave is reflected instantly and the incident overpressure is intensified. Subsequently, the reflection wave quickly declined. It is also concluded that the pressure–time curve recorded by gauge 3 abruptly increases to relatively high pressure because the explosive products flow into the field, which was first occupied by sandwich panels.

### 4.3 Deformation pattern and velocity response

In this subsection, the numerical results for deformation pattern and velocity response are described in terms of the front face sheet, the core, and the back face sheet based on the configuration of the sandwich panels.

**Fig. 17** Effect of graded polyurethane foam core strategy on the permanent deflection

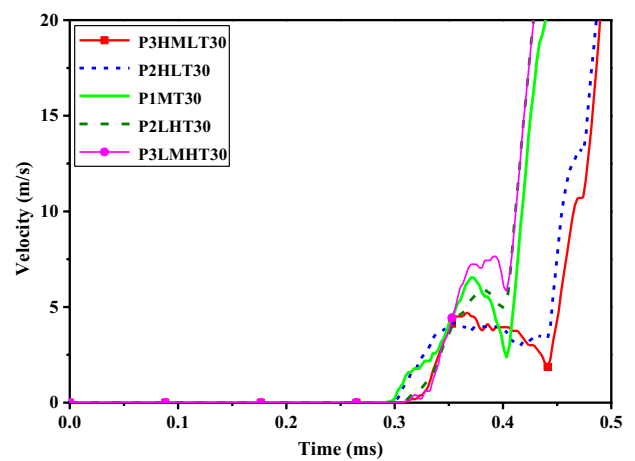
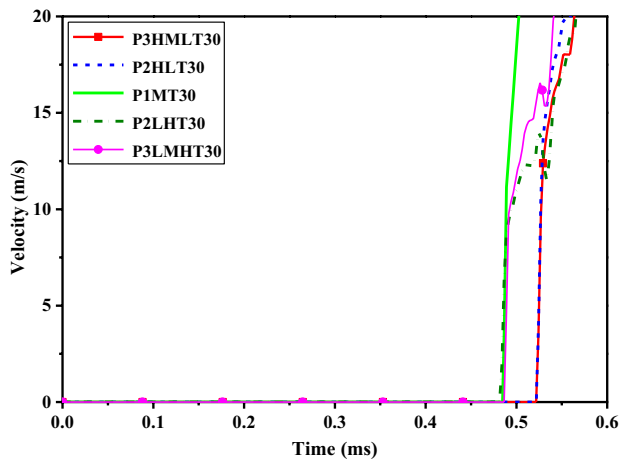
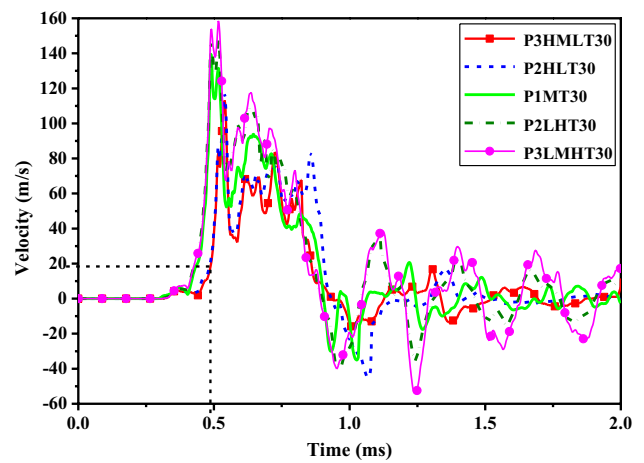
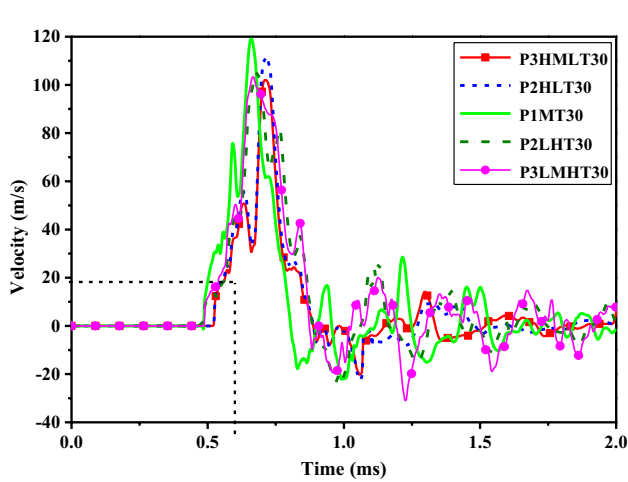
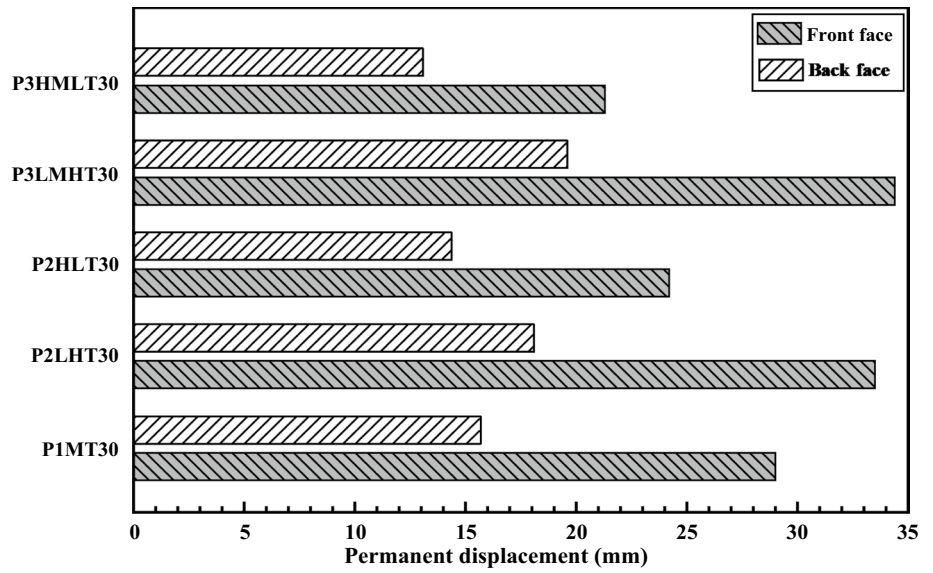


**Fig. 18** Velocity–time history of the back face sheets for all panels at the center point (enlarged review of 0–600  $\mu$ s)

**Fig. 19** Velocity–time history of the front face sheets for all panels at the center point (enlarged review of 0–500  $\mu$ s)

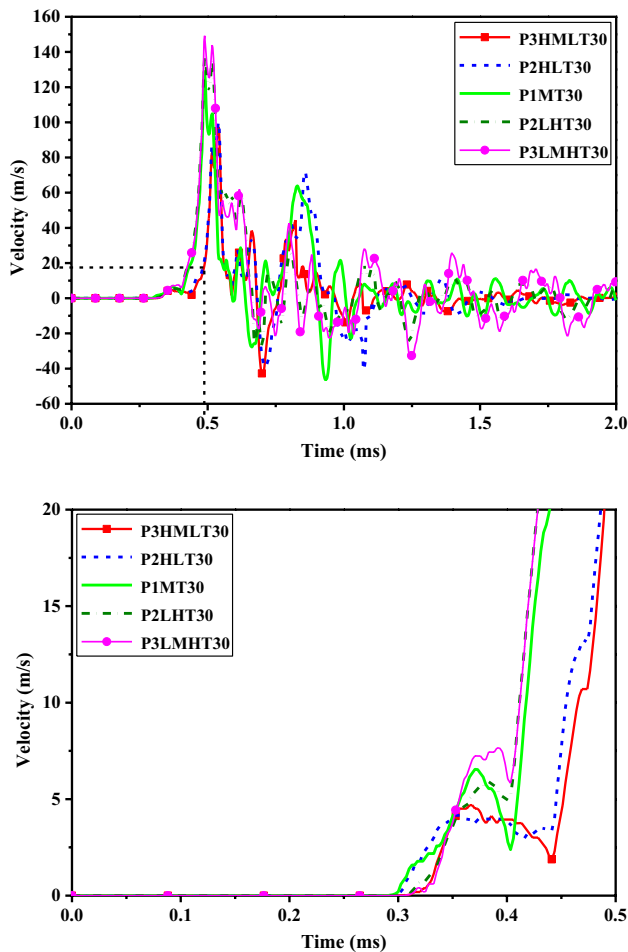


**Fig. 20** Velocity–time history of the core for all panels at the center point (enlarged review of 0–500  $\mu$ s)

Figures 14, 15, 16 show the displacement–time history of the back and front face sheets and the core at the center point along with an enlarged review of 0–600  $\mu$ s, respectively. It should be mentioned that in Fig. 16, the difference between the permanent deflections of the front and back face sheets was considered as the core compression amount. The results show that in P3HMLT30, P2HLT30, P1MT30, P2LHT30, and P3LMHT30 configurations, deformations of the back face sheet commence at 527  $\mu$ s, 527  $\mu$ s, 489  $\mu$ s, 489  $\mu$ s, and 491  $\mu$ s, respectively, then gradually increase and approach a plateau of 14.2 mm, 15.6 mm, 17.2 mm, 19.3 mm, and 20.1 mm at approximately 888  $\mu$ s, 888  $\mu$ s, 804  $\mu$ s, 885  $\mu$ s, and 873  $\mu$ s, respectively. Afterward, an oscillation is observed until the panel rests. It is represented that the deflection of the front face sheet enhances at a faster pace than the rate at which the back face sheet deforms. In these configurations, core crushing starts at 308  $\mu$ s, 300  $\mu$ s, 295  $\mu$ s, 308  $\mu$ s, and 310  $\mu$ s, respectively, and the curves go up sharply until about 681  $\mu$ s, 683  $\mu$ s, 637  $\mu$ s, 663  $\mu$ s, and 658  $\mu$ s, respectively.

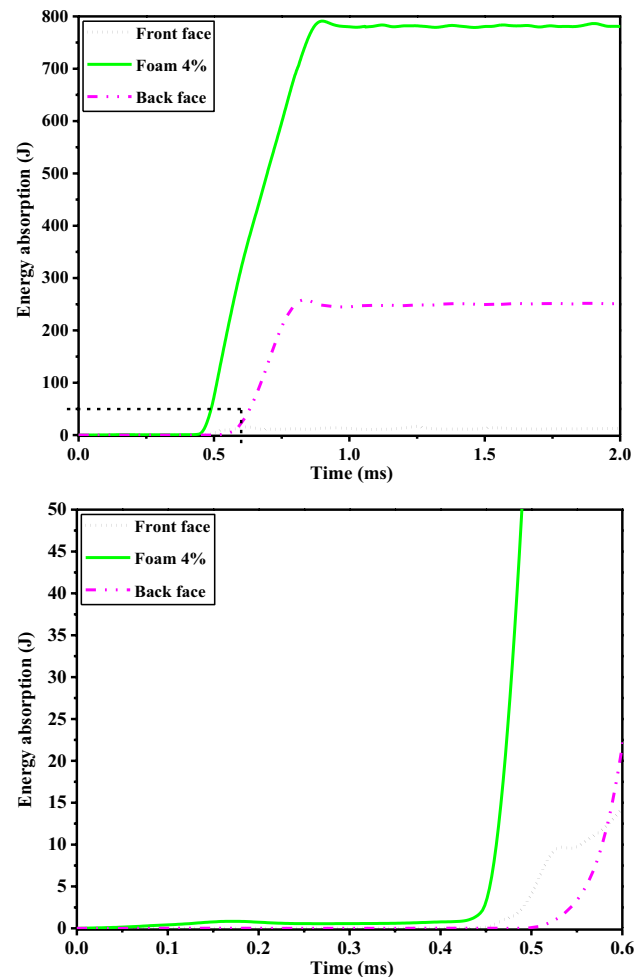


**Fig. 21** Plastic energy dissipation–time history of P1MT30 at the center point (enlarged review of 0–600  $\mu$ s)

Then, the crushing speed becomes much slower, and the curves approach the maximum value at 2 ms, which is the permanent core compression. It can be also inferred from the curves that although the layering arrangement has an obvious influence on the transient and permanent deflection response of face sheets and core, increasing the number of core layers does not significantly change the response of the core.

For better understanding, the influence of graded polyurethane foam core strategy on the back and front face sheets' permanent deflections of panels is illustrated in Fig. 17. It is obvious that the front and back face sheet deflections of P3HMLT30 are smaller than other sandwich panels, especially P3LMHT30, and changing the direction of core layers in the sandwich panel, as well as an increase of the number of the core layers, play a vital role on mitigation of back and front face sheet deflections. In other words, employing a high-density core as the first core layer of the sandwich panel along with increasing the number of core layers leads

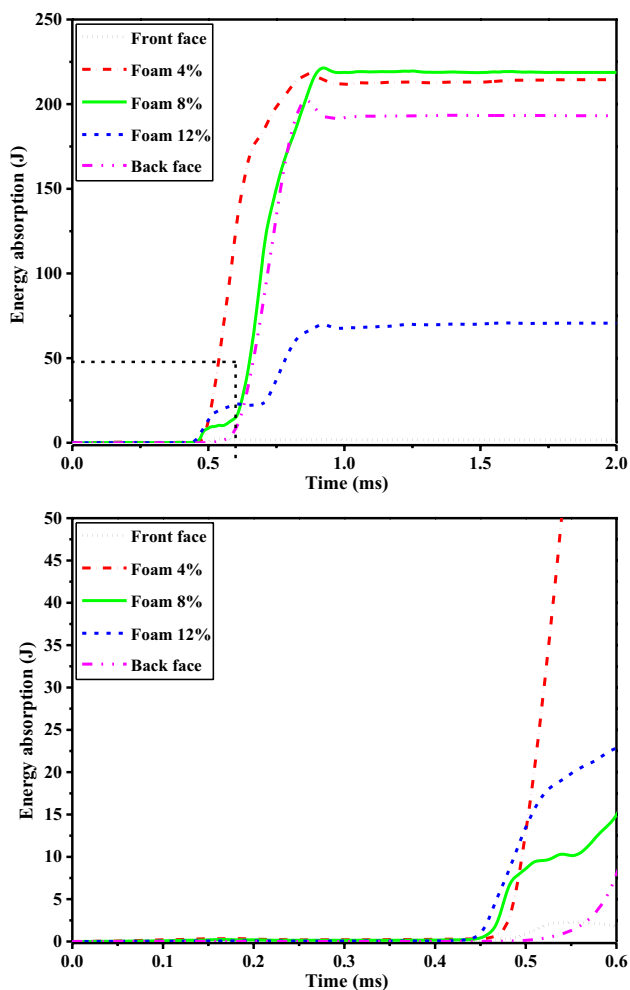


**Fig. 22** Plastic energy dissipation–time history of P3HMLT30 at the center point (enlarged review of 0–600  $\mu$ s)

to the dissipation of more kinetic energy by suffering crushing deformation. A closer look on Fig. 17 represents that the blast performance with regard to the permanent deflections of the back and front face sheets could be classified as an ascending sequence, as follows: P3HMLT30, P2HLT30, P1MT30, P2LHT30, and P3LMHT30 configuration. Using the back face sheet deflection of the P1MT30 configuration as a benchmark, P3HMLT30 and P2HLT30 configurations give a decrease by 16.8% and 8.3%, respectively, while P2LHT30 and P3LMHT30 configurations give an increase by 15.4% and 25%, respectively. Also, using the front face sheet deflection of the P1MT30 configuration as a benchmark, P3HMLT30 and P2HLT30 configurations give a decrease by 26.6% and 16.6%, respectively, while P2LHT30 and P3LMHT30 configurations give an increase by 15.5% and 18.6%, respectively.

To analyze the dynamic plastic response of the sandwich panels, the velocity–time history of the back and front face

sheets and the core at the center point are considered. Figures 18, 19, 20 illustrate the curves of all sandwich panels along with an enlarged review of specific time duration. As shown in Figs. 18, 19, 20, the back face sheet of P3HMLT30, P2HLT30, P1MT30, P2LHT30, and P3LMHT30 configurations commences to move and accelerate constantly at the time same as the displacement–time curves. The front face sheet of each sandwich panel begins to move and accelerate at a faster rate in comparison with the back face sheet before the above-mentioned time values. Subsequently, the velocity of the back and front face sheet abruptly decreases, and afterward, an oscillation is observed until the panels rest. The sudden drop in the velocity of the back face sheet is due to the fact that the deformed front face sheet impacts the back face sheet directly, which indicates the emergence of the slapping mechanism. This phenomenon also shows that no failure occurred during the slapping process because the velocity of face sheets decreases suddenly and there were no constant values for velocity in a specific period of time. A closer look on these figures proves that the characteristics of the velocity–time curves of the P3HMLT30, P2HLT30, P2LHT30, and P3LMHT30 sandwich panels are a closer resemblance to P1MT30 and the graded polyurethane foam core strategy does not affect the velocity curve. Using the P1MT30 configuration as a benchmark, the graded polyurethane foam core induces a decrease of back face sheet peak velocity by 14.2%, 6.3%, 11.3%, and 13.3% for P3HMLT30, P2HLT30, P2LHT30, and P3LMHT30 configurations, respectively. The percentage differences in front face sheet peak velocity are -18.9%, -15.8%, 6.1%, and 13.6% for the above-mentioned configurations, respectively.

#### 4.4 Energy absorption capacity

For clarification of the inherent mechanism underlying the dynamic plastic deformation response, energy absorption specifications of sandwich panels are inspected in this subsection. Figure 21 and Fig. 22 show the plastic energy dissipation–time history of P1MT30 and P3HMLT30 configurations at the center point along with an enlarged review of 0–600  $\mu$ s, respectively. As shown in these figures, at the primary response stage, before 500  $\mu$ s, the front face sheet and polyurethane foam core first absorb the blast energy, whereas the plastic energy dissipated by the back face sheet is approximately zero. Afterward, the energy dissipated by each constituent gradually increases and approaches a plateau value. It is noteworthy to mention that the back face sheet starts as an energy absorber, while the slapping phenomenon occurs. For the case of the P3HMLT30 configuration, different core layers share the task of energy absorption from inception. A comparison between P1MT30 and P3HMLT30 configurations clearly shows that using graded polyurethane foam core strategy

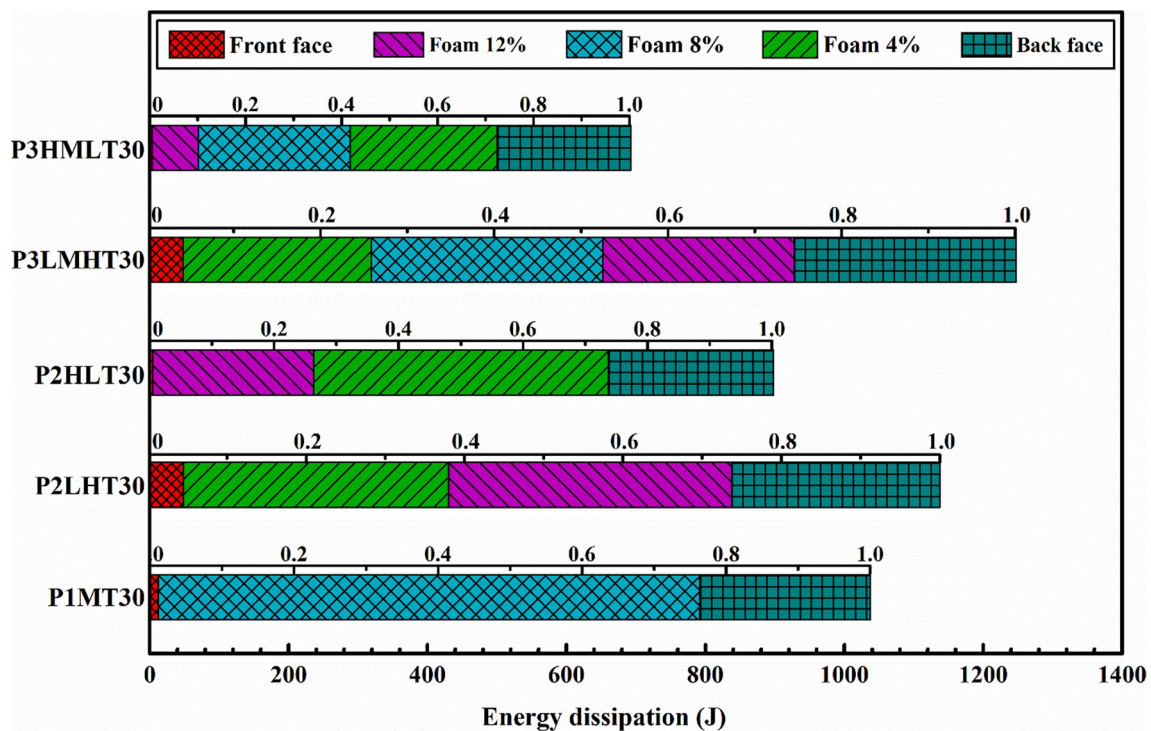


**Fig. 23** Effect of graded polyurethane foam core strategy on the energy dissipation

in descending order in terms of relative density (HML) reduces the plastic energy absorption of both face sheets and polyurethane foam core.

For better understanding, the stacked bar diagram is used to analyze the plastic energy absorbed by different constituents of a sandwich panel, as shown in Fig. 23. To quantify the contribution of panel constituents, the numbers ranging from 0 to 1 with a distance of 0.2 were placed upon each stacked bar.

Using the plastic energy absorbed by the P1MT30 configuration as a benchmark, P3HMLT30 and P2HLT30 configurations give a decrease by 30.2% and 13.8%, respectively, while P2LHT30 and P3LMHT30 configurations give an increase by 32.9% and 42.2%, respectively. Also, using the plastic energy absorbed by the core of the P1MT30 configuration as a benchmark, P3HMLT30 and P2HLT30 configurations give a decrease by 33.8% and 12.6%, respectively, while P2LHT30 and P3LMHT30 configurations give an increase by 1% and 7.4%, respectively. It is noteworthy to mention that in the P2HLT30 and P3HMLT30 configurations, due to the presence of a higher-density material as the first core layer of the sandwich structure, the energy absorbed by the front face sheet is approximately zero.

## 5 Conclusion

In this study, by using an explosive shock tube apparatus, a series of experiments were carried out to analyze the blast-resistant behavior of metallic sandwich panels with graded polyurethane foam cores subjected to blast loading. For this, different types of core configurations were examined, while the mass and thickness of the panel were constant. The first configuration consisted of a single-layered polyurethane core with an average density ratio of 8%, while the second and third configurations comprised a double-layered and triple-layered core. It is noteworthy to mention that in the second and third arrangements, the back and front face sheets swapped their positions. The permanent deflections of face sheets at the center were measured in the experiments. All the sandwich panels exhibited an analogous plastic deformation mode, which was characterized by a uniform global dome with the maximum transverse deflection taking place at the center of the panel. According to the results obtained from experimental investigations, a corresponding numerical simulation study was proposed using the explicit analysis code ANSYS/Autodyn. The main contributions of the current numerical study have studied the influence of graded



polyurethane foam core strategy on the deformation modes and velocity responses fluid–structure interaction effect, and energy absorption capacity of sandwich panels. The following results were found:

- By using the back face sheet deflection of the P1MT30 configuration as a benchmark, P3HMLT30 and P2HLT30 configurations gave a decrease, while P2LHT30 and P3LMHT30 configurations gave an increase.
- By using the P1MT30 configuration as a benchmark, the graded polyurethane foam core induced a decrease in back face sheet peak velocity for P3HMLT30, P2HLT30, P2LHT30, and P3LMHT30 configurations.
- By using the plastic energy absorbed by the back face sheet of the P1MT30 configuration as a benchmark, P3HMLT30 and P2HLT30 configurations gave a decrease, while P2LHT30 and P3LMHT30 configurations gave an increase.
- By comparing P1MT30 and P3HMLT30 configurations, it was found that using graded polyurethane foam core strategy in descending order in terms of relative density (HML) reduces the plastic energy absorption of both face sheets and polyurethane foam core. Besides, in the P2HLT30 and P3HMLT30 configurations, due to the presence of a higher-density material as the first core layer of the sandwich structure, the energy absorbed by the front face sheet is approximately zero.
- By considering the aforementioned results, the blast-resistant behaviors of sandwich panels with different graded polyurethane foam core strategies were classified from the best to worst by taking the permanent deflection of the back face sheet as an index, as follows: P3HMLT30, P2HLT30, P1MT30, P2LHT30, and P3LMHT30.

## References

1. Huang W et al (2016) Dynamic response and failure of PVC foam core metallic sandwich subjected to underwater impulsive loading. *Compos B Eng* 97:226–238
2. Huang W et al (2019) Impulsive response of composite sandwich structure with tetrahedral truss core. *Compos Sci Technol* 176:17–28
3. Langdon GS et al (2018) The influence of interfacial bonding on the response of lightweight aluminium and glass fibre metal laminate panels subjected to air-blast loading. *Proc Inst Mech Eng C J Mech Eng Sci* 232(8):1402–1417
4. Mostofi TM et al (2019) Large transverse deformation of double-layered rectangular plates subjected to gas mixture detonation load. *Int J Impact Eng* 125:93–106
5. Rezasefat M, Mostofi TM, Ozbakkaloglu T (2019) Repeated localized impulsive loading on monolithic and multi-layered metallic plates. *Thin-Walled Struct* 144:106332
6. Mostofi TM et al (2020) Gas mixture detonation load on polyurea-coated aluminum plates. *Thin-Walled Struct* 155:106851
7. Ziya-Shamami M et al (2020) Structural response of monolithic and multi-layered circular metallic plates under repeated uniformly distributed impulsive loading: an experimental study. *Thin-Walled Struct* 157:107024
8. Behtaj M, Babaei H, Mostofi TM (2022) Repeated uniform blast loading on welded mild steel rectangular plates. *Thin-Walled Struct* 178:109523
9. Mostofi TM, Babaei H, Alitavoli M (2016) Theoretical analysis on the effect of uniform and localized impulsive loading on the dynamic plastic behaviour of fully clamped thin quadrangular plates. *Thin-Walled Struct* 109:367–376
10. Yazici M et al (2014) Experimental and numerical study of foam filled corrugated core steel sandwich structures subjected to blast loading. *Compos Struct* 110:98–109
11. Zhang P et al (2016) Experimental study on the dynamic response of foam-filled corrugated core sandwich panels subjected to air blast loading. *Compos B Eng* 105:67–81
12. Karagiozova D et al (2016) The influence of a low density foam sandwich core on the response of a partially confined steel cylinder to internal air-blast. *Int J Impact Eng* 92:32–49
13. Wang A et al (2022) Dynamic response of sandwich tubes with continuously density-graded aluminium foam cores under internal explosion load. *Materials* 15(19):6966
14. Xia Y et al (2016) Protective effect of graded density aluminium foam on RC slab under blast loading—an experimental study. *Constr Build Mater* 111:209–222
15. Chen Y et al (2016) Transient underwater shock response of sacrificed coating with continuous density graded foam core. *Compos B Eng* 98:297–307
16. Gardner N, Wang E, Shukla A (2012) Performance of functionally graded sandwich composite beams under shock wave loading. *Compos Struct* 94(5):1755–1770
17. Li S et al (2015) Finite element simulation of metallic cylindrical sandwich shells with graded aluminium tubular cores subjected to internal blast loading. *Int J Mech Sci* 96:1–12
18. Li S et al (2017) Sandwich panels with layered graded aluminium honeycomb cores under blast loading. *Compos Struct* 173:242–254
19. Yang L et al (2018) Numerical investigations on blast resistance of sandwich panels with multilayered graded hourglass lattice cores. *J Sandwich Struct Mater* 5:109
20. Kelly M et al (2016) Sandwich panel cores for blast applications: materials and graded density. *Exp Mech* 56(4):523–544
21. Chen Y et al (2015) Mitigating performance of elastic graded polymer foam coating subjected to underwater shock. *Compos B Eng* 69:484–495
22. Liang M et al (2017) Blast resistance and design of sandwich cylinder with graded foam cores based on the Voronoi algorithm. *Thin-Walled Struct* 112:98–106
23. Mostafa HE, El-Dakhkhni WW, Mekky WF (2010) Use of reinforced rigid polyurethane foam for blast hazard mitigation. *J Reinf Plast Compos* 29(20):3048–3057
24. Langdon G et al (2012) The response of sandwich structures with composite face sheets and polymer foam cores to air-blast loading: preliminary experiments. *Eng Struct* 36:104–112
25. Langdon G et al (2013) The air-blast response of sandwich panels with composite face sheets and polymer foam cores: experiments and predictions. *Int J Impact Eng* 54:64–82

26. Rajaneesh A, Sridhar I, Rajendran S (2014) Relative performance of metal and polymeric foam sandwich plates under low velocity impact. *Int J Impact Eng* 65:126–136
27. Zhou J et al (2012) The low velocity impact response of foam-based sandwich panels. *Compos Sci Technol* 72(14):1781–1790
28. Zhou J, Guan Z, Cantwell W (2013) The impact response of graded foam sandwich structures. *Compos Struct* 97:370–377
29. Ye N et al (2017) Dynamic response and failure of sandwich plates with PVC foam core subjected to impulsive loading. *Int J Impact Eng* 109:121–130
30. Doğru M, Güzelbey İ (2018) Investigation of the impact effects of thermoplastic polyurethane reinforced with multi-walled carbon nanotube for soldier boot under the blast load. *J Therm Compos Mater* 5:908
31. Rashad M, Yang T (2018) Numerical study of steel sandwich plates with RPF and VR cores materials under free air blast loads. *Steel Compos Struct* 27(6):717–725
32. Mishra SK, Shukla DK, Patel RK (2018) Flexural properties of functionally graded epoxy-alumina polymer nanocomposite. *Mater Today Proc* 5(2):8431–8435
33. Aydin M et al (2014) An experimental study on ballistics performance: functionally graded sandwich plate impacted by a 9 mm parabolium projectile. *Blucher Mat Sci Proc* 1(1):1–4
34. Hohe J et al (2012) Numerical and experimental design of graded cellular sandwich cores for multi-functional aerospace applications. *Mater Des* 39:20–32
35. Lin Q, Chen F, Yin H (2017) Experimental and theoretical investigation of the thermo-mechanical deformation of a functionally graded panel. *Eng Struct* 138:17–26
36. Brırsan M et al (2013) Mechanical behavior of sandwich composite beams made of foams and functionally graded materials. *Int J Solids Struct* 50(3–4):519–530
37. Garg A, Chalak H, Chakrabarti A (2020) Comparative study on the bending of sandwich FGM beams made up of different material variation laws using refined layerwise theory. *Mech Mater* 151:103634
38. Jing L et al (2019) Experimental and numerical study of sandwich beams with layered-gradient foam cores under low-velocity impact. *Thin-Walled Struct* 135:227–244
39. Sun G et al (2018) Low-velocity impact behaviour of sandwich panels with homogeneous and stepwise graded foam cores. *Mater Des* 160:1117–1136
40. Seyedkanani A, Niknam H, Akbarzadeh A (2020) Bending behavior of optimally graded 3D printed cellular beams. *Addit Manuf* 35:101327
41. Bocciarelli M, Bolzon G, Maier G (2006) Three-Point-bending and indentation tests for the calibration of functionally graded material models by inverse analysis. In: *III European Conference on Computational Mechanics*. Springer
42. Czechowski L (2019) Study on strength and stiffness of WC-Co-NiCr graded samples. *Materials* 12(24):4166
43. Li C, Shen H-S, Wang H (2019) Thermal post-buckling of sandwich beams with functionally graded negative Poisson's ratio honeycomb core. *Int J Mech Sci* 152:289–297
44. Xiao D et al (2019) Compression behavior of the graded metallic auxetic reentrant honeycomb: experiment and finite element analysis. *Mater Sci Eng, A* 758:163–171
45. Jin X et al (2016) Dynamic response of sandwich structures with graded auxetic honeycomb cores under blast loading. *Compos B Eng* 106:206–217
46. Chen D, Jing L, Yang F (2019) Optimal design of sandwich panels with layered-gradient aluminum foam cores under air-blast loading. *Compos B Eng* 166:169–186
47. Zhou X, Jing L (2020) Deflection analysis of clamped square sandwich panels with layered-gradient foam cores under blast loading. *Thin-Walled Struct* 157:107141
48. Jing L et al (2021) Experimental and numerical study of square sandwich panels with layered-gradient foam cores to air-blast loading. *Thin-Walled Struct* 161:107445
49. Lee E, Hornig H, Kury J (1968) *Adiabatic expansion of high explosive detonation products*. Univ. of California Radiation Lab. at Livermore, Livermore
50. Rogers GFC, Mayhew YR (1981) *Thermodynamic and transport properties of fluids*. Blackwell, Oxford
51. Dobratz B (1981) *LLNL explosives handbook: properties of chemical explosives and explosives and explosive simulants*. Lawrence Livermore National Lab., CA (USA)
52. AUTODYN T (2003) *Theory Manual Revision 4.3*, Concord, CA: Century Dynamics. Inc.
53. Sharma A et al (2018) Deformation behavior of single and multi-layered materials under impact loading. *Thin-Walled Struct* 126:193–204
54. Steinberg D (1996) *Equation of state and strength properties of selected materials*. Springer, Berlin
55. Chen W, Lu F, Winfree N (2002) High-strain-rate compressive behavior of a rigid polyurethane foam with various densities. *Exp Mech* 42(1):65–73
56. Andami H, Toopchi-Nezhad H (2020) Performance assessment of rigid polyurethane foam core sandwich panels under blast loading. *Int J Prot Struct* 11(1):109–130
57. Saha M et al (2005) Effect of density, microstructure, and strain rate on compression behavior of polymeric foams. *Mater Sci Eng A* 406(1–2):328–336
58. Johnson GR, Cook WH (1985) Fracture characteristics of three metals subjected to various strains, strain rates, temperatures and pressures. *Eng Fract Mech* 21(1):31–48
59. Mabrouki T, Rigal J-F (2006) A contribution to a qualitative understanding of thermo-mechanical effects during chip formation in hard turning. *J Mater Process Technol* 176(1–3):214–221
60. Elek PM et al (2016) Experimental and numerical investigation of perforation of thin steel plates by deformable steel penetrators. *Thin-Walled Struct* 102:58–67
61. Rezasefat M et al (2019) Dynamic plastic response of double-layered circular metallic plates due to localized impulsive loading. *Proc Inst Mech Eng Part L J Mater Des Appl* 233(7):1449–1471
62. Luccioni B et al (2018) Experimental and numerical analysis of blast response of High Strength Fiber Reinforced Concrete slabs. *Eng Struct* 175:113–122
63. Tan P (2014) Ballistic protection performance of curved armor systems with or without debondings/delaminations. *Mater Des* 64:25–34

**Publisher's Note** Springer Nature remains neutral with regard to jurisdictional claims in published maps and institutional affiliations.

Springer Nature or its licensor (e.g. a society or other partner) holds exclusive rights to this article under a publishing agreement with the author(s) or other rightsholder(s); author self-archiving of the accepted manuscript version of this article is solely governed by the terms of such publishing agreement and applicable law.